










Multicolor Variability of Young Stars in the Lagoon Nebula: Driving Causes and Intrinsic Timescales

Laura Venuti^{1,8,9} , Ann Marie Cody² , Luisa M. Rebull³ , Giacomo Beccari⁴ , Mike J. Irwin⁵ , Sowmya Thanvantri⁶,
Steve B. Howell¹ , and Geert Barentsen⁷ 

¹ NASA Ames Research Center, Moffett Boulevard, Mountain View, CA 94035, USA; lvenuti@seti.org

² SETI Institute, 189 Bernardo Avenue, Suite 200, Mountain View, CA 94043, USA

³ Infrared Science Archive (IRSA), IPAC, 1200 E. California Boulevard, California Institute of Technology, Pasadena, CA 91125, USA

⁴ European Southern Observatory, Karl-Schwarzschild-Strasse 2, D-85748 Garching bei München, Germany

⁵ Institute of Astronomy, University of Cambridge, Madingley Road, Cambridge, CB3 0HA, UK

⁶ University of California, Berkeley, 101 Sproul Hall, Berkeley, CA 94720, USA

⁷ Bay Area Environmental Research Institute, 625 2nd Street, Suite 209, Petaluma, CA 94952, USA

Received 2021 March 23; revised 2021 May 9; accepted 2021 May 21; published 2021 August 13

Abstract

Space observatories have provided unprecedented depictions of the many variability behaviors typical of low-mass, young stars. However, those studies have so far largely omitted more massive objects ($\sim 2 M_{\odot}$ to $4\text{--}5 M_{\odot}$) and were limited by the absence of simultaneous, multiwavelength information. We present a new study of young star variability in the $\sim 1\text{--}2$ Myr old, massive Lagoon Nebula region. Our sample encompasses 278 young, late B to K-type stars, monitored with Kepler/K2. Auxiliary u , g , r , i , $H\alpha$ time-series photometry, simultaneous with K2, was acquired at the Paranal Observatory. We employed this comprehensive data set and archival infrared photometry to determine individual stellar parameters, assess the presence of circumstellar disks, and tie the variability behaviors to inner disk dynamics. We found significant mass-dependent trends in variability properties, with B/A stars displaying substantially reduced levels of variability compared to G/K stars for any light-curve morphology. These properties suggest different magnetic field structures at the surface of early-type and later-type stars. We also detected a dearth of some disk-driven variability behaviors, particularly dippers, among stars earlier than G. This indicates that their higher surface temperatures and more chaotic magnetic fields prevent the formation and survival of inner disk dust structures corotating with the star. Finally, we examined the characteristic variability timescales within each light curve and determined that the day-to-week timescales are predominant over the K2 time series. These reflect distinct processes and locations in the inner disk environment, from intense accretion triggered by instabilities in the innermost disk regions to variable accretion efficiency in the outer magnetosphere.

Unified Astronomy Thesaurus concepts: [Young stellar objects \(1834\)](#); [Circumstellar disks \(235\)](#); [Variable stars \(1761\)](#); [Young star clusters \(1833\)](#); [Multi-color photometry \(1077\)](#); [Time series analysis \(1916\)](#)

Supporting material: machine-readable table

1. Introduction

The few million years (Myr) age mark represents a crucial juncture in stellar evolution, when newly formed protostars emerge from their nebular cocoon, become optically visible, and enter the pre-main-sequence (PMS) track. The physics of young stellar objects (YSOs) during these early stages is dominated by the interaction between the central star and the surrounding disk of gas and dust, a ubiquitous outcome of the star formation process (e.g., Shu et al. 1987; McKee & Ostriker 2007). The exchange of mass and angular momentum between the star and the disk, regulated via the process of magnetospheric accretion (e.g., Hartmann et al. 2016), has a profound impact on the long-term evolution of the star. The dynamics of star-disk interaction is also directly relevant to the process of planet formation, by triggering changes in the local disk structure (e.g., Morbidelli & Raymond 2016, and references therein) and by influencing planetary migration and the location of “planet traps” across the disk (Romanova et al. 2019).

While the past few years have witnessed a true revolution in protoplanetary disk surveys with the Atacama Large Millimeter/

submillimeter Array (ALMA; e.g., Ansdell et al. 2016b; Barenfeld et al. 2016), the spatial scales of the inner disk region relevant to magnetospheric star-disk interactions ($\lesssim 0.1$ au; Dullemond & Monnier 2010) are hard to resolve with current facilities, even for the YSOs closest to us (Andrews et al. 2016). To date, mapping the star-disk emission across the spectrum and tracing the variability of the observed emission features represent the most direct probes to disclose the physics of the star-inner disk environment. In particular, observations in the ultraviolet (UV) reveal any energetic emission from accretion shocks that form when streams of material are channeled from the inner disk onto the star (e.g., Calvet & Gullbring 1998; Gullbring et al. 1998; Schneider et al. 2020, and references therein). The accelerated gas in magnetospheric accretion funnels are also associated with distinctive spectroscopic signatures such as $H\alpha$ line emission (e.g., White & Basri 2003; Kurosawa et al. 2006). Observations in the optical, sensitive to the photospheric emission from the central star, allow us to reconstruct any modulation effects by surface features (e.g., Bouvier et al. 1995; Grankin et al. 2008) or circumstellar structures (e.g., Bouvier et al. 2007; Fonseca et al. 2014; Frasca et al. 2020). Finally, infrared (IR) wavelengths trace the thermal emission produced by dust at different locations within the disk, from the inner au (near-IR; e.g., Robberto et al. 2010; Roquette et al. 2020), to radii of a few au (mid-IR; e.g.,

⁸ NASA Postdoctoral Program Fellow.

⁹ Now at SETI Institute, 189 Bernardo Avenue, Suite 200, Mountain View, CA 94043, USA.

Oliveira & van Loon 2004; Günther et al. 2014), to tens of au (far-IR; e.g., Fedele et al. 2013; Alonso-Martínez et al. 2017).

Although young stars have long been known to be strongly variable sources (e.g., Joy 1945), and although numerous photometric and spectroscopic monitoring campaigns of young stars have been conducted from ground-based facilities down to timescales of minutes (e.g., Bastian & Mundt 1979a, 1979b), time-series data before the era of space observatories did not possess the cadence, duration, and precision required to categorize different YSO behaviors beyond the assertion of periodic versus irregular versus extinction-driven variability patterns (Herbst et al. 1994). The paradigm began to shift with the Microvariability and Oscillations of Stars (MOST) telescope (Walker et al. 2003), the Spitzer Space Telescope (Werner et al. 2004), and the Convection, Rotation, and planetary Transits (CoRoT) telescope (Baglin 2003; Auvergne et al. 2009). The accuracy and homogeneity of space data enabled showcasing YSO variability as a panchromatic phenomenon (e.g., Morales-Calderón et al. 2011), which can appear with characteristic features on timescales as short as hours (e.g., Rucinski et al. 2008). Although not sensitive to the eruptive variability events typical of EXors and FUors, which take place over years-long timescales (Audard et al. 2014), those space-based, high-cadence data sets enabled detailing, for the first time, the distinct hour-to-month light-curve morphology classes characteristic of young, disk-bearing stars (Alencar et al. 2010) and brought to light a larger variety of behaviors than could be appreciated from the ground.

The current framework for time-domain studies of young stars was first established by the Coordinated Synoptic Investigation of NGC 2264 (CSI 2264; Cody et al. 2014). The campaign employed CoRoT and Spitzer, in coordination with a dozen other space- and ground-based observatories, to monitor the hour-to-week variability of hundreds of low-mass YSOs in the 3–5 Myr old cluster NGC 2264 (Dahm 2008). The quality of space-based data enabled the implementation of quantitative metrics to classify light-curve behaviors and their occurrence rates. Multiwavelength data gathered from the ground in the UV (Venuti et al. 2014, 2015) and in the $H\alpha$ band (Sousa et al. 2016) enabled assessing the connection between distinct variability features and disk-related phenomena. The original census of YSO behaviors was expanded from a few categories to at least eight, including two separate irregular patterns, named bursters (dominated by brightening events; Stauffer et al. 2014) and stochastic (Stauffer et al. 2016), and a variety of morphologies for light curves dominated by fading events, the so-called dippers (Stauffer et al. 2015; McGinnis et al. 2015). Bursting and stochastic behaviors were interpreted as the imprint of intense, unstable, and/or time-variable accretion, as earlier predicted from a theoretical standpoint by Kulkarni & Romanova (2008) and Kurosawa & Romanova (2013). Dipping behaviors were interpreted as the result of repeated partial occultations of the stellar surface by intervening inner disk warps, or by dust entrained in accretion columns, in star–disk systems observed at intermediate to high inclinations (i.e., close to edge-on). Regular, (quasi-)periodic behaviors, also common among the investigated YSOs, were ascribed to modulation by dark magnetic spots or bright accretion spots at the stellar surface.

The paradigm for YSO variability that emerged from CSI 2264 was later tested and expanded in studies of (among others) the ~ 8 Myr old Upper Scorpius (Preibisch & Mamajek 2008) and the ~ 2 Myr old ρ Ophiucus (Wilking et al. 2008), targeted as part of the K2 mission (Howell et al. 2014) with the Kepler spacecraft

(Borucki et al. 2010). Such studies led to (i) identifying new subclasses among periodic variables, possibly driven by warm gas clouds corotating with the star after the inner disk has been cleared (Stauffer et al. 2017); (ii) establishing a homogeneous pattern of rotational evolution across the PMS (Rebull et al. 2018, 2020); (iii) characterizing the duty cycle, duration, and timescales of bursting events in irregular variables, in connection with different models of episodic accretion (Cody et al. 2017); and (iv) exploring YSO variability properties in relation to inner disk radii and outer disk inclinations (Cody & Hillenbrand 2018), in synergy with ALMA surveys of protoplanetary disks (Carpenter et al. 2014; Barenfeld et al. 2017). However, those results were obtained mainly for low-mass YSOs ($\lesssim 1.5 M_{\odot}$; spectral type K and M). Higher-mass young stars are known to be variable as well (e.g., Teixeira et al. 2018), but the frequencies and detailed morphologies of their light-curve types have yet to be explored. Moreover, our understanding of YSO behaviors, as shaped during CSI 2264 and early K2 campaigns, pivots on the role of the stellar magnetic field, both in driving spot-modulated variability and in governing accretion-dominated variability. However, while magnetic fields are detected ubiquitously among low-mass YSOs, they are rarely found on intermediate-mass YSOs and Herbig Ae/Be stars that lack a convective envelope (Villebrun et al. 2019). This may suggest that different variability properties or mechanisms are to be expected for higher-mass YSOs. Another limitation of earlier K2 surveys was the absence of auxiliary multiwavelength data, gathered simultaneously. Indeed, while space data provide an unprecedented view of the morphology of flux variations exhibited by YSOs on various timescales, multiwavelength information is crucial to reconstruct the spectrum of the luminosity variations and to pinpoint their physical origin (e.g., Vrba et al. 1993; Venuti et al. 2015, and references therein).

In this work, we address the issues listed above by conducting a thorough analysis of YSO variability in the Lagoon Nebula region, a rich H II region located in the Sagittarius arm of our Galaxy (Tothill et al. 2008). Much of its PMS population is contained in the open cluster NGC 6530, an extremely young ($0.7_{-0.4}^{+0.9}$ Myr; Prisinzano et al. 2019) star-forming region situated in the heart of the Lagoon Nebula, at a distance of ~ 1325 pc (Damiani et al. 2019). The region hosts a comparatively higher mass population than other young clusters studied earlier, including numerous O and B stars. The Lagoon Nebula was observed with Kepler as part of the K2 Campaign 9, and other telescopes were employed at the same time to sample the variability of Lagoon Nebula YSOs at different wavelengths: the Very Large Telescope (VLT) of the European Southern Observatory (ESO), with its spectrograph FLAMES (Fibre Large Array Multi Element Spectrograph; Pasquini et al. 2000), to probe the spectroscopic $H\alpha$ variability; and the VLT Survey Telescope (VST), with its wide-field imager OmegaCAM (Kuijken 2011), to probe the color variability of Lagoon Nebula YSOs in u , g , r , i , and narrowband $H\alpha$ filters. We use here the K2 and VST/OmegaCAM data to measure the amount of multicolor variability and to reconstruct the color behaviors exhibited by different categories of YSO variables in our sample, in relation to stellar and circumstellar properties. The analysis of spectroscopic variability is deferred to a later work.

The paper is organized as follows. Section 2 describes our target selection, the time-series photometric data collected with Kepler/K2 and VST/OmegaCAM, and the literature information used to complement our own data set (notably in the IR). In Section 3, we illustrate the methods used to derive individual

stellar properties (extinction, spectral types) and to identify disk-bearing and disk-free YSOs in our sample. In Section 4, we examine the variability properties exhibited by Lagoon Nebula YSOs in K2 and VST/OmegaCAM filters: the morphological classification of K2 light curves as a function of disk status and spectral type (Section 4.1); the correlated variability exhibited by young stars in our sample at different wavelengths (u , r , i , $H\alpha$), as a function of luminosity (Section 4.2); and the connection between K2 variability types and stellar colors at UV, optical, and IR wavelengths, which trace disk-related phenomena (Section 4.3). In Section 5, we investigate the color variation trends associated with prominent flux variability features in the K2 light curves for disk-bearing YSOs and discuss their implications for the magnetospheric accretion and star-disk interaction structure around different types of variables. In Section 6, we conduct a structure function analysis of the K2 light curves to extract the characteristic timescales of variability for all YSO categories in our sample, and we explore the dominant types of signal (white noise, flicker noise, Brownian noise, sinusoidal variations) that govern the time series, as well as the time spans on which they emerge. In Section 7 we discuss our results in relation to mass-dependent stellar internal structure, circumstellar dust structure, and magnetic field properties; we also examine their implications for the stability of the circumstellar environment at, and beyond, the inner disk. Our conclusions are summarized in Section 8.

2. Target Selection and Observational Data

2.1. The Lagoon Nebula Region in the Literature

The Lagoon Nebula is a benchmark for investigations of early stellar evolution and to probe the conditions for planet formation, thanks to the very young age of the NGC 6530 cluster and to its rich population of PMS stars that span a wide range of masses. As such, the region has been extensively studied over the past decades with a variety of diagnostics, and over 35 published papers or survey catalogs exist to date that encompass the NGC 6530 region. These include the Massive Young star-forming complex Study in Infrared and X-ray (MYStIX; Kuhn et al. 2013), the Gaia survey (Damiani et al. 2019), the Gaia-ESO Survey (GES; Prisinzano et al. 2019; Wright et al. 2019), the Panoramic Survey Telescope and Rapid Response System (Pan-STARRS; Chambers et al. 2016; Flewelling et al. 2020), and the VST Photometric $H\alpha$ Survey of the Southern Galactic Plane and Bulge (VPHAS+; Kalari et al. 2015) in the optical and the UKIRT Infrared Deep Sky Survey (UKIDSS; Lawrence et al. 2007), the Two Micron All Sky Survey (2MASS; Skrutskie et al. 2006), Spitzer data including the Galactic Legacy Infrared Mid-Plane Survey Extraordinaire (GLIMPSE; Churchwell et al. 2009) and the Spitzer Enhanced Imaging Products (SEIP) archive, and Wide-field Infrared Survey Explorer (WISE; Wright et al. 2010) data in the IR. We cross-matched all of the existing Lagoon Nebula catalogs in the literature, to build an extensive sample of probable and candidate members based on any diagnostics of stellar youth or PMS status (which include enhanced X-ray emission related to magnetic activity, UV and $H\alpha$ emission related to accretion processes, IR flux emission related to thermal emission from the disk, lithium absorption indicative of youth, and astrometric association with the cluster). In total, we found ~ 3000 YSO candidates, out of which ~ 1000 – 1500 candidate members projected onto the area covered by the K2 mosaic. This

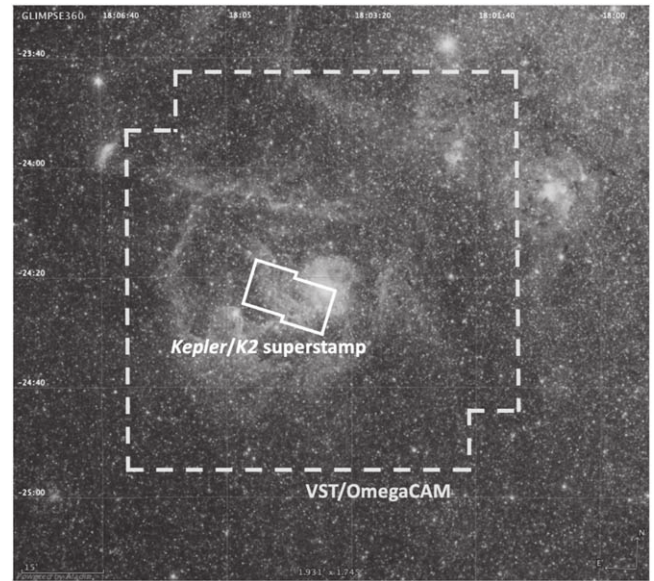


Figure 1. Black-and-white image of the Lagoon Nebula field from Spitzer/GLIMPSE, over which the total area covered with VST/OmegaCAM (sum of two dithered pointings) and the Kepler/K2 superstamp region are outlined as dashed and solid contours, respectively. The original version of the background image was prepared with Aladin Desktop (Bonnarel et al. 2000).

number includes very faint or embedded sources, detected only in the IR. Around 700 candidate members possess an optical counterpart in the literature and have corresponding Kepler magnitudes ranging from 8 to 20 (spectral types B to M, or masses between 5 and $0.2 M_{\odot}$). After filtering down in magnitude to ensure sufficient signal-to-noise ratio in K2 photometry, we retained a list of ~ 300 YSOs, primarily located toward the NGC 6530 cluster core.

2.2. K2 Observations

K2 monitored the Lagoon Nebula from 2016 April 21 through July 1. The campaign was split into two segments, with an interruption of nearly 4 days between May 18 and 22. The bulk of the NGC 6530 cluster was observed as a K2 “superstamp” region (see Figure 1), for which a $\sim 15' \times 9'$ image was acquired every 6.5 s. Sets of 270 frames were then co-added for an ultimate cadence of roughly 30 minutes. Additional data were acquired simultaneously for 11 stars outside the superstamp region.

To generate light curves, we performed photometry with circular apertures ranging in radii from 1 to 4 pixels. Kepler’s pointing was unstable on ~ 6 hr timescales during the K2 mission, and thus it is important to recenter the apertures in each successive image. For superstamp targets (i.e., the majority of our targets), we accomplished this by converting stars’ known R.A. and decl. into pixel position using an accurate world coordinate system (WCS) transformation, as described by Cody et al. (2018). For non-superstamp targets, we computed a flux-weighted centroid as described in Cody & Hillenbrand (2018).

Once an aperture was centered, we summed the flux and subtracted out the median background as determined in a 10×10 pixel region surrounding the source center, with outliers iteratively removed. After performing the aperture photometry, we selected the preferred light curve by visually examining the set of four produced for each star. If there were no nearby companions on the image, then we chose the

Table 1Young Stars Targeted during K2 Campaign 9 in the Lagoon Nebula Core, and Multiband u , g , r , i , $H\alpha$ Photometry in the Vega System Gathered for Each Source with VST/OmegaCAM

EPIC ID ^a	2MASS ID	Spectral Class ^b	A_V	Disk Flag ^c	u -mag	g -mag	r -mag	i -mag	$H\alpha$ -mag	K2 Class ^d
224366753	J18034826-2422233	Late G	0.5	?	17.04	15.52	14.49	14.01	14.09	P
224355341	J18034935-2423374	Mid K	0.3	N	19.22	17.47	16.18	15.62	15.51	P
224378426	J18035006-2421079	Early K	0.1	N	17.28	15.22	14.17	13.72	13.99	QPS
224379624	J18035063-2421001	Late B	0.3	N	13.14	12.36	12.32	12.29	12.28	U
224361254	J18035221-2422592	Early K	0.5	N	16.25	14.34	13.23	12.71	12.98	MP

Note. The table is published in its entirety in the machine-readable format. A portion is shown here for guidance regarding its form and content.

^a Identification number for the target from the Ecliptic Plane Input Catalog, if available.

^b Approximate spectral class derived for each target as described in Section 3.1. The mention of “Early” encompasses spectral subclasses 0 to 3, “Mid-” corresponds to subclasses 4 to 6, and “Late” identifies subclasses 7 to 9.

^c Possible flag values are “Y” if the target is a disk-bearing YSO, “N” if the target is a disk-free object, and “?” if the spectral energy distribution of the object and the disk indicators described in Section 3.2 provide contrasting or incomplete information. In our analysis, we consider objects labeled “?” as disk candidate YSOs.

^d Morphological class of the K2 light curve for the target. Possible values for this field are “P” (periodic), “QPS” (quasi-periodic symmetric), “S” (stochastic), “B” (burster), “QPD” (quasi-periodic dipper), “APD” (aperiodic dipper), “MP” (multi-periodic), “EB” (eclipsing binary), “N” (nonvariable), and “U” (unclassifiable), as detailed in Section 4.1.

(This table is available in its entirety in machine-readable form.)

aperture that produced the least noisy light curve. However, if there were one or more close companions, we chose the aperture least subject to flux contamination. In cases for which contamination could not be avoided and the origin of variability was unknown, we eliminated that object from our sample. This process left us with a total of 278 stars with sufficient-quality K2 light curves. This sample of Lagoon Nebula YSOs, which is nearly complete down to magnitudes $V \sim 16.5$ – 17 , constitutes the focus of our work and is listed in Table 1.

2.3. VST/OmegaCAM Data Set

The VST/OmegaCAM run on the Lagoon Nebula field was executed over a period of 3.5 weeks (2016 June 16 through July 10; Program ID 297.C-5033(A), PI Cody), partly overlapping with the second half of the K2 run. Seventeen observing epochs were obtained, distributed over 14 nonconsecutive days. Each observing block comprised two dithered exposures in the Sloan Digital Sky Survey (SDSS) u , g , r , i filters (Figure 1) and three dithered exposures in a narrowband, 659 nm $H\alpha$ filter (Drew et al. 2014). Each set of exposures per filter was repeated twice, once with longer exposure times (70 s in u , 5 s in g , 4 s in r and i , and 30 s in $H\alpha$) and once with very short exposure times (1 s in u , 0.3 s in g , r and i , and 0.5 s in $H\alpha$), to recover the brightest (B-type) stars in our field that would be saturated in exposures of a few seconds or less, particularly in the red filters. On the two nights when more than one observing epoch was acquired, the distinct epochs were separated by a lag of 20 minutes to 1 hr. All frames were processed using the Cambridge Astronomy Survey Unit (CASU) pipeline, and point-source catalogs were produced for each band and exposure. All single-epoch catalogs were then cross-matched to produce light curves. Only sources that were detected in at least 10 separate exposures were retained for the light-curve production. A total of 187,530 sources were retrieved, with light curves in at least one VST band; among these, 2444 are included in the list of candidate YSOs compiled as described in Section 2.1.

The instrumental photometry was calibrated to SDSS magnitudes in the Vega system by cross-correlating the list of average magnitudes for all point sources in our VST survey with the catalog of the Lagoon Nebula region published by the

consortium of the VPHAS+ project, which was conducted using the same instrument. The photometric calibration was ultimately performed on a sample of 29,492 objects, common to our VST catalog and to the VPHAS+ catalog, and comprising only field stars (not YSO candidates). No significant color effects were observed; hence, the calibration was performed band by band to correct only for zero-point offsets. For each filter, a 10σ -clipping routine was performed to reject outliers affected by very large photometric discrepancies between our catalog and the VPHAS+ catalog. Then, the zero-point correction was calculated as the typical magnitude difference measured, across the remaining sample, between our catalog and the VPHAS+ catalog, while the rms dispersion around this value was extracted as uncertainty on our zero-point correction. The resulting magnitude corrections are listed in Equation (1), and the average calibrated photometry for the sample of YSOs investigated in this study is reported in Table 1.

$$\begin{aligned}
 u - u_{\text{VPHAS+}} &= 7.55 \pm 0.07 \\
 g - g_{\text{VPHAS+}} &= 5.30 \pm 0.04 \\
 r - r_{\text{VPHAS+}} &= 5.43 \pm 0.03 \\
 i - i_{\text{VPHAS+}} &= 5.88 \pm 0.05 \\
 H\alpha - H\alpha_{\text{VPHAS+}} &= 8.31 \pm 0.09.
 \end{aligned} \tag{1}$$

Since the processes we aim to investigate (dynamics of disk accretion, star–disk interaction, stellar activity) develop primarily over timescales from hours to weeks (e.g., Grankin et al. 2008; Costigan et al. 2014), we decided to retain, in our VST time-series analysis, only the error-weighted average magnitudes measured for each observing epoch in each VST filter, in order to reduce the impact of photometric scatter within individual observing blocks. The final VST time series used for the analysis therefore comprise 17 photometric measurements, taken at separations between ~ 0.5 hr and 5 days from one another. In addition, plots of the light-curve rms versus average magnitude were inspected in all filters to identify the brightness limit above which the trend starts to diverge from the expected behavior of decreasing light-curve noise for increasing brightness (e.g., Moraux et al. 2013; Venuti et al. 2015). Examples of such plots for the u band and the r band are shown in Figure 2 (left and right panels, respectively).

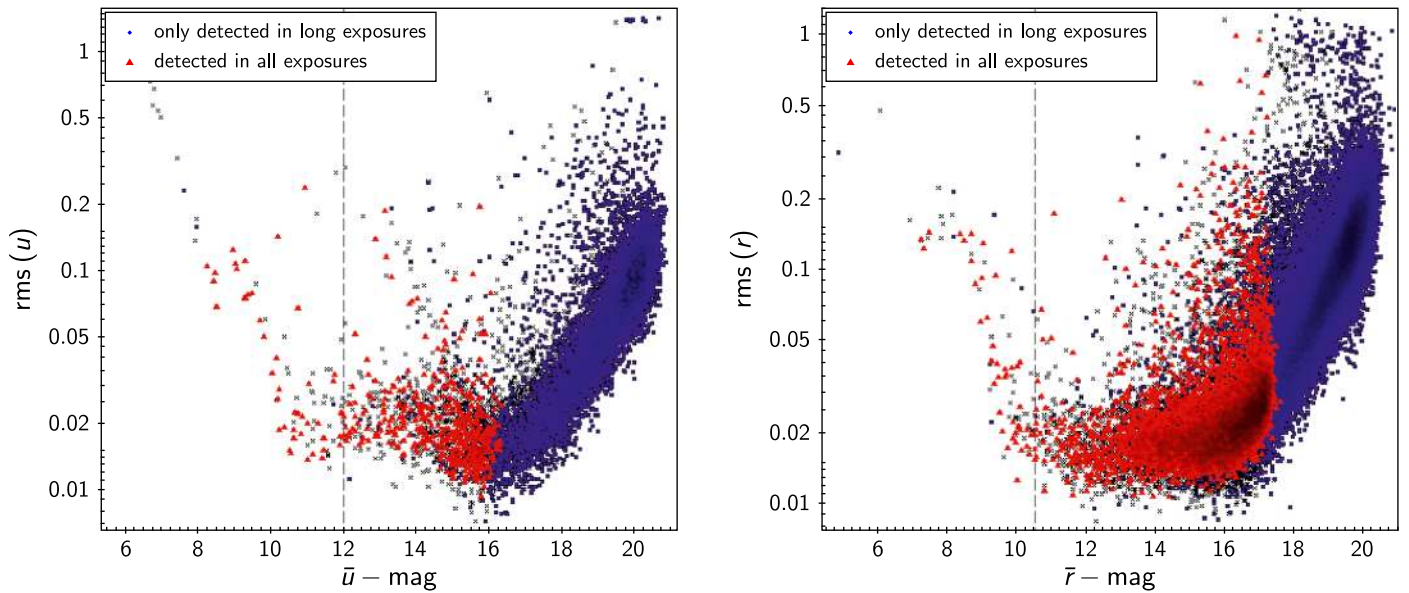


Figure 2. The rms dispersion measured in VST/OmegaCAM u -band (left) and r -band (right) light curves for all point sources in the Lagoon Nebula field, as a function of the average light-curve magnitude. Objects marked as blue diamonds correspond to sources that were detected only in the long exposures (see Section 2.3), while objects marked as red triangles correspond to sources detected in all exposures of each observing block. The dashed gray line marks the estimated saturation limit below which sources were discarded.

For magnitudes $\bar{u} \gtrsim 16$, the measured light-curve rms scatter increases exponentially for increasing (fainter) magnitudes, consistent with expectations. A trend reversal is observed for $\bar{u} < 16$, where the measured rms slightly increases for decreasing magnitudes and then remains approximately constant down to $\bar{u} \sim 12$. This trend reversal can be explained by the fact that objects fainter than $\bar{u} \sim 16$ were only detected in the long exposures, while objects brighter than $\bar{u} \sim 16$ were mostly detected in all exposures, with potentially different accuracy depending on the exposure time. A similar effect, albeit less pronounced, can be observed on the $\text{rms}(r)$ versus \bar{r} diagram. Nevertheless, these distinct behaviors between brighter stars and fainter stars do not affect our statistical analysis of variability described later, as we have only considered error-weighted average magnitudes for each exposure block (composed of two dithered long exposures and two dithered short exposures), as indicated above. Moreover, in our statistical assessment of variability properties (see, in particular, Section 4.2), each group of objects (e.g., disk-bearing YSOs, disk-free YSOs) was weighted against other stellar groups (field stars, different types of YSOs) in the same magnitude range, therefore ensuring a self-consistent analysis on a relative scale. On the other hand, Figure 2 also shows a tail of bright objects, at $\bar{u} \leq 12$ and $\bar{r} \leq 10.5$, which appear to diverge from the trend traced by stars down to magnitudes ~ 15 . We suspect that these objects may be close to or past the saturation limit, and therefore we discarded all sources to the left of the dashed gray lines on the diagrams. Similar cuts were applied in the other bands, at $\bar{g} = 11$, $\bar{i} = 11$, and $\overline{H\alpha} = 10.5$.

2.4. Additional Catalogs Used for This Work

In order to reconstruct the properties of the circumstellar environment for our target stars, we complemented our optical/UV data sets with IR data from literature surveys mentioned in Section 2.1. In the near-IR, we gathered J , H , K data from the 2MASS and UKIDSS catalogs, which encompass $\sim 90\%$ of the Lagoon Nebula YSOs for which K2 photometry could be

extracted. In the mid-IR, we gathered data obtained with the Infrared Array Camera (IRAC) on board Spitzer at 3.6, 4.5, 5.8, and 8.0 μm , available for 75% of the K2 sample (Kumar & Anandarao 2010; Povich et al. 2013; Broos et al. 2013, and references therein). More specifically, to assign IRAC magnitudes to each of our targets, we prioritized extracting all four photometric measurements in IRAC bands from the same source for each given star and used, in order, the data released by SEIP, MYStIX, GLIMPSE, or Kumar & Anandarao (2010). When no IRAC photometry from any sources was available, we downloaded the SEIP images of our targets' field of view and extracted our own aperture photometry measurements (L. Rebull et al., 2021 in preparation). As a consistency check, we extended this procedure to targets with photometry already provided in the archival catalogs, and we could ascertain that the derived magnitudes typically agree within 0.05–0.10 mag. We also gathered available data from the WISE catalog at wavelengths from 3.4 to 22 μm , albeit only for a quarter of our target list. We used this IR data set to sort our targets into disk-bearing and disk-free sources, as detailed in Section 3.2. In addition, we collected optical photometry in standard Johnson–Cousins filters (notably V , R , and I ; e.g., van den Ancker et al. 1997; Sung et al. 2000; Prisinzano et al. 2005), which we used for the selection of IR excess sources, as also described in Section 3.2.

3. Stellar and Circumstellar Properties of Young Stars in the Lagoon Nebula

Of the 278 objects in our K2 sample, each has a counterpart in the VST catalog, with a median separation of $0''.15$ and a maximum separation of $1''.27$ from the spatial coordinates of the K2 detection. We used the collected multiwavelength photometry to inspect the location of each object on various color–color diagrams, in order to evaluate key stellar properties such as spectral type and to assess the disk status of each YSO, as reported in the following.

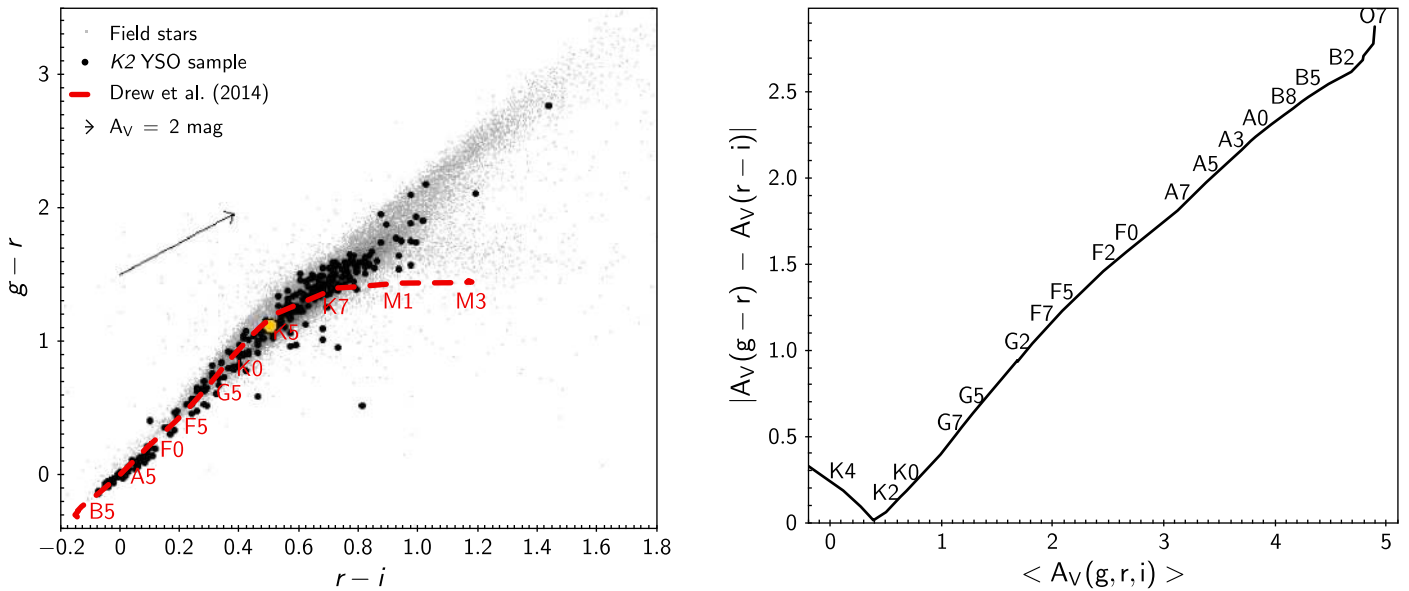


Figure 3. Left: typical VST g , r , i colors of Lagoon Nebula members monitored with K2 (black circles), overlaid on the color distribution of field stars (gray circles). The sequence of synthetic, nonreddened colors tabulated in Drew et al. (2014) is dashed in red as a reference, and the location of representative SpTs is labeled along the sequence to guide the reader. The extinction vector shown on the diagram corresponds to $A_V = 2$ mag following a nonstandard reddening law with $R_V = 5$. A yellow circle marks the object for which results of the A_V derivation are shown as an example in the right panel. Right: average A_V measured from $r - i$ and $g - r$ colors, and absolute difference between the corresponding $A_V(r - i)$ and $A_V(g - r)$, calculated for the object marked in yellow on the left panel with respect to the nonreddened colors tabulated for each SpT in Drew et al. (2014), and labeled as a reference along the A_V curve. The spectral type that minimizes the difference $|A_V(g - r) - A_V(r - i)|$ is extracted as the best SpT estimate, and the corresponding average $\langle A_V(g, r, i) \rangle$ is extracted as the best estimate of individual A_V .

3.1. Individual Extinction and Spectral Type Estimates

To assign estimates of individual extinction (A_V) and of spectral type (SpT) homogeneously across our sample, we used the g , r , i colors provided by our VST data set. We did not include u -band or $H\alpha$ -band data for this step of the analysis, as they may be affected by accretion activity in these young sources. Similarly, we did not include IR data for the determination of stellar parameters, as they may be affected by thermal emission from the disk. To derive the best photometric estimate of A_V and the corresponding photospheric SpT for each object, we assumed an anomalous reddening law $R_V = 5.0$ toward NGC 6530 members, as reported in Prisinzano et al. (2019), and adopted the sequence of synthetic, nonreddened colors for dwarfs tabulated in VPHAS+ bands by Drew et al. (2014), as shown in Figure 3.

For each object, we calculated what value of A_V would be required to correct the observed $r - i$ and $g - r$ colors, in order to match the nonreddened colors tabulated for any given spectral subclass across the mid-O to mid-M range. This calculation was conducted independently on the two colors, using the nonstandard reddening law mentioned earlier. We then selected as the best SpT estimate the class for which the computed $A_V(r - i)$ and $A_V(g - r)$ exhibit the closest agreement. We estimated an rms uncertainty of 0.19 mag on the measured A_V , ensuing from the uncertainties on the photometry calibration (Equation (1)). Therefore, negative A_V solutions greater than -0.19 were considered consistent with $A_V \sim 0$; conversely, solutions where the minimum absolute difference $|A_V(r - i) - A_V(g - r)|$ corresponds to an average $\langle A_V(g, r, i) \rangle$ lower than -0.19 and those with minimum $|A_V(r - i) - A_V(g - r)|$ larger than $3 \times \text{rms} = 0.57$ mag were discarded.

When implementing the procedure outlined above using the instantaneous $g - r$ and $r - i$ colors measured at the various VST monitoring epochs, individual estimates of the apparent spectral type can deviate by as much as one class above or below the typical range of SpT derived for each star. In order to

assign a robust estimate of SpT to each object, we extracted a best-fit SpT from the average photometric properties detected for each source during the VST monitoring and considered as uncertainty the typical dispersion around this value derived from individual observing epochs, mostly on the order of a few spectral subclasses. By following this approach, we were able to assign an SpT estimate to $\sim 81\%$ of our sample: among these, $\sim 7\%$ were categorized as B-type stars, $\sim 13\%$ as A-type, $\sim 8\%$ as F-type, $\sim 17\%$ as G-type, and $\sim 55\%$ as K-type. No SpT could be measured for the remaining sources owing to a degeneracy between the observed color properties and the adopted extinction law, or because the best SpT estimates obtained in those cases from $r - i$ and $g - r$ colors did not agree within the accepted ranges discussed above.

Approximate spectral classes and estimated A_V values for our targets, derived as described here, are reported in Table 1.

3.2. Selection of Disk-bearing Stars

To assess whether the young stars in our sample are surrounded by thick inner disks, or whether they have already cleared their close surroundings, we employed a variety of diagnostics. As a first step, we conducted a visual inspection of the spectral energy distribution (SED) of each object with a K2 light curve, from UV to mid-IR wavelengths, to detect any excess emission at IR wavelengths above the flux level of the stellar photosphere (e.g., Robitaille et al. 2007). This analysis resulted in a preliminary classification of our objects as Class II sources (which exhibit significant excess emission at wavelengths longer than $\sim 2 \mu\text{m}$, originated in a circumstellar disk) or Class III sources (with little or no flux contribution from circumstellar dust), as originally proposed by Lada (1987). We then corroborated our classification by investigating the IR color properties of our stars with respect to several disk indicators, as enumerated below.

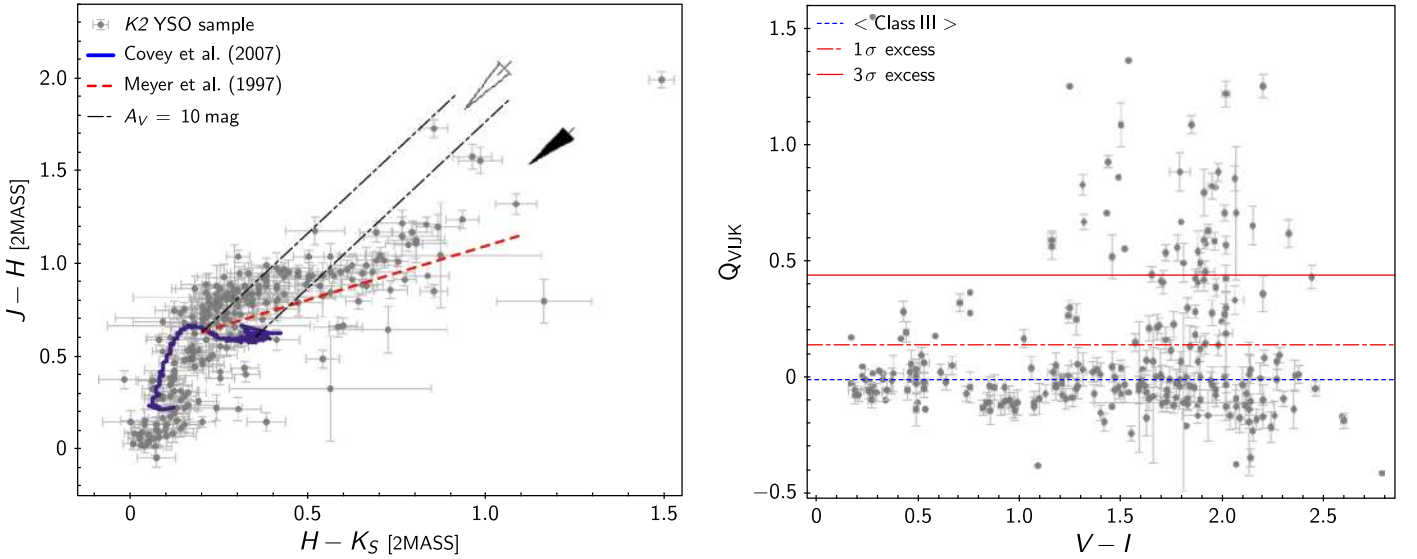


Figure 4. Left: 2MASS J, H, K color-color diagram for young stars in the Lagoon Nebula, monitored with K2. The blue curve traces the dwarf color locus tabulated in Covey et al. (2007). The dashed red line traces the disk-bearing YSO locus defined in Meyer et al. (1997). The dashed-dotted black lines trace a 10 mag reddening vector starting from the beginning of the Meyer locus and from the end of the dwarf sequence. Objects above (or consistent with) the Meyer locus and that fall in the area indicated by the black arrow, to the right of the second black line, were classified as disk-bearing sources; objects above (or consistent with) the Meyer locus and that fall in the area indicated by the white arrow, between the first and second black lines, were classified as disk candidates. Right: Q_{VIJK} index calculated for young stars in the Lagoon Nebula, shown against their $V - I$ colors. The dotted blue line traces the typical Q_{VIJK} value measured for Class III sources in the sample, while the dashed-dotted and solid red lines mark a 1σ level and a 3σ level above the Class III threshold, respectively. Objects that fall above the solid line were classified as disk-bearing sources, while those that fall between the dotted and the dashed-dotted lines were classified as disk candidates according to this indicator.

1. We used the 2MASS and UKIDSS data to build the J, H, K color-color diagram, which is sensitive to dust in the innermost disk regions, at distances <0.1 au from the central star. The resulting diagram is illustrated in Figure 4 (left panel). Young stars with significant excess emission in J, H, K bands are expected to distribute along a separate color locus from stars that exhibit purely photospheric emission, as discussed in Meyer et al. (1997).
2. We investigated the photometric properties of our stars in the wavelength range probed by Spitzer/IRAC filters ($3.6\text{--}8.0\ \mu\text{m}$; also see Section 4.3.1 below), sensitive to thermal emission from dust within the inner au around solar-type stars, and verified which of the targets exhibit colors consistent with the Class II locus defined by Allen et al. (2004).
3. We used the WISE photometry, when available, to build color-color diagrams in the W1 ($3.4\ \mu\text{m}$), W2 ($4.6\ \mu\text{m}$), and W3 ($12\ \mu\text{m}$) passbands, and we ascertained which sources exhibit color properties consistent with the Class II locus defined by Koenig & Leisawitz (2014).
4. We calculated two reddening-free indices, Q_{JHK} and Q_{VIJK} , defined by Damiani et al. (2006) as

$$Q_{JHK} = (J - H) - \frac{A(J - H)}{A(H - K)}(H - K) \quad (2)$$

$$Q_{VIJK} = (J - K) - \frac{A(J - K)}{A(V - I)}(V - I). \quad (3)$$

Such indices provide a measure of the near-IR color excess exhibited by disk-bearing stars with respect to disk-free stars in the region, computed after normalizing the cluster locus to the reddening direction on the color-color diagram. For each of the two indices, the typical photospheric value was defined as the average measured across K2 targets in the Lagoon Nebula that were

classified as Class III sources upon a visual inspection of their SED. All objects that fell at a distance of over 3σ with respect to the typical Class III value were then classified as disk sources, while objects that fell at a distance of $1\sigma\text{--}3\sigma$ from the typical Class III locus were classified as disk candidates (Figure 4, right panel).

Classifications from each indicator were then combined to assign a final disk status to each target: objects visually classified as Class II SEDs that satisfy at least another IR excess indicator were retained as disk-bearing sources; objects visually classified as Class III SEDs that do not exhibit any IR excess indicator were retained as disk-free sources; objects with discordant classifications or incomplete information, due to missing data, among the various indicators were flagged as potential disk candidates. Disk-bearing sources account for $\sim 31\%$ of our sample, disk-free sources for $\sim 50\%$, and potential disk candidates for $\sim 19\%$.

Table 2 reports how the fractions of disk-bearing, disk-free, and disk candidate stars in our sample vary as a function of spectral class. The disk fraction does not appear to be uniform across the Lagoon Nebula population but appears to be higher among later-type stars. In order to estimate an uncertainty on the measured disk fractions and to evaluate the impact of sample incompleteness, we used the results of our SpT and disk classification analysis on the sample with K2 data to derive the occurrence rates of each spectral class and disk class as a function of R magnitudes for the entire population of YSO candidates in the Lagoon Nebula region identified in our literature mining effort (see Section 2.1). More specifically, we selected, among the ~ 3000 YSO candidates identified from the literature, those with Johnson-Cousins R -band magnitudes or SDSS r -band magnitudes (statistically calibrated to R -magnitudes) in the range $R \sim 8\text{--}17.5$, within which our K2 targets are distributed. This selection produced a sample of ~ 1100 YSO candidates. From our K2 targets, classified in SpT and disk status as described in Sections 3.1 and 3.2, respectively, we

Table 2

Percentage of Disk-bearing, Disk-free, and Disk Candidate Members of the Lagoon Nebula Region, Monitored with K2, as a Function of Their Spectral Class

Spectral Class	Disk-bearing	Disk Candidates	Disk-free
B-type	13% $^{+0\%}_{-2\%}$ [23% \pm 7%]	31% $^{+4\%}_{-3\%}$ [31% \pm 4%]	56% $^{+5\%}_{-3\%}$ [46% \pm 5%]
A-type	17% $^{+3\%}_{-3\%}$ [39% \pm 4%]	23% $^{+7\%}_{-3\%}$ [15% \pm 1%]	60% $^{+5\%}_{-7\%}$ [46% \pm 4%]
F-type	12% $^{+5\%}_{-2\%}$ [32% \pm 7%]	18% $^{+5\%}_{-3\%}$ [21% \pm 2%]	70% $^{+3\%}_{-7\%}$ [47% \pm 6%]
G-type	31% $^{+5\%}_{-4\%}$ [37% \pm 4%]	20% $^{+2\%}_{-3\%}$ [19% \pm 2%]	49% $^{+6\%}_{-5\%}$ [44% \pm 4%]
K-type	36% $^{+7\%}_{-4\%}$ [56% \pm 3%]	16% $^{+3\%}_{-3\%}$ [17% \pm 1%]	48% $^{+4\%}_{-7\%}$ [27% \pm 2%]

Note. Values reported outside the square brackets correspond to the statistics measured from our targets with an available SpT estimate from the analysis in Section 3.1, and the associated uncertainties are derived from the subsample of targets with no SpT estimate. The percentages given in square brackets are projected statistics that account for the population of YSO candidates in the same magnitude range as our targets, but with no K2 photometry (hence not included in this study).

measured the statistical frequencies of different spectral classes and disk classes as a function of R and estimated the associated errors from the subset of objects in our sample with no SpT estimate. We then used these statistical frequencies and associated errors to randomly sample the population of ~ 1100 YSO candidates selected upon their R -band or r -band magnitudes, as described above, but with no K2 data. At each sampling, we randomly selected magnitude-dependent SpT frequencies from the frequency distributions extracted from our targets and determined a statistical estimate of disk-bearing, disk-free, and disk candidate objects for each spectral class across the entire population of YSO candidates. The average disk fractions obtained with this procedure in 250 random samplings, as well as the associated standard deviations, are also reported in Table 2.

4. The Variability Properties of Young Stars in the Lagoon Nebula

In this section we provide a characterization of the diverse variability behaviors exhibited by young stars in the Lagoon Nebula region. In Section 4.1, we describe the classification scheme that we adopted to assign a label to each K2 light curve based on the dominant morphological pattern of the observed flux variations. In Section 4.2, we employ the simultaneous VST time-series photometry to evaluate the amount of correlated variability exhibited by our targets at optical and UV wavelengths, as a function of optical brightness and of the K2 variability type. In Section 4.3, we explore the color properties of our targets on multiple photometric diagrams to pinpoint the physical origin of the observed variability behaviors.

4.1. K2 Light-curve Morphology Classes

To sort our sample of K2 light curves into morphological classes, we adopted the metrics developed by Cody et al. (2014) as part of the CSI2264 project. The classification scheme is based on two indicators that probe two distinct properties of the light curves: the degree of periodicity or stochasticity of the luminosity pattern, and the degree of symmetry (i.e., the balance between brightening and fading trends) of the observed flux variations with respect to the typical luminosity state of the object. Eight main categories of variables are identified with this scheme:

1. *periodic* (P), which exhibit repeated, sinusoidal-like flux patterns with little or no evolution in shape or amplitude from one cycle to the next;

2. *quasi-periodic symmetric* (QPS), which exhibit an overall periodic flux pattern, symmetric in amplitude below and above the typical luminosity level of the star, but with noticeable changes in shape and/or amplitude from one cycle to the next;
3. *stochastic* (S), which exhibit irregular flux variations with no apparent periodicity and no preference for brightening events over fading events or vice versa;
4. *bursters* (B), which exhibit irregular flux variations, prominently in the form of intense and short-lived brightening events on top of a flat or slowly varying light-curve continuum, occurring with no obvious periodicity but repeatedly over spans of days or weeks;
5. *quasi-periodic dippers* (QPD), which exhibit prominent fading events, in a recurring pattern with a detectable periodicity, although with changes in shape and depth from one cycle to the next;
6. *aperiodic dippers* (APD), which exhibit prominent fading events, possibly repeated but with no obvious periodicity along the time series;
7. *multi-periodic* (MP), which exhibit multiple periodicities (e.g., a beating pattern or pulsations);
8. *eclipsing binaries* (EB), which exhibit the characteristic photometric signatures of one companion transiting the other, superimposed on the out-of-eclipse individual variability patterns.

Additional groupings include *flat-line* or nonvariable light curves (N), which exhibit no appreciable day-to-week variability patterns beyond statistical fluctuations, and *unclassifiable* patterns (U), which do not match any of the classes defined above. Representative examples of light curves belonging to different variability classes are illustrated in Figure 5.

As can be seen, the intensity of flux variations is markedly different for distinct variable classes. Across our sample, regular variables like MP, QPS, and P sources, driven by magnetic starspots, possibly mixed with stable accretion spots, exhibit median peak-to-peak amplitudes (with $>10\sigma$ flux outliers removed) of order 12%, 19%, and 26%, respectively, compared to the average flux level. While some underlying starspot variability is expected across all variable groups, this would constitute only a minor component in the most irregular photometric behaviors. Indeed, S variables exhibit median flux amplitudes $\sim 55\%$, followed by QPD variables (78%), APD variables (93%), and B variables (125%). Flat-line light curves, instead, merely exhibit median photometric fluctuations of order 3% in flux.

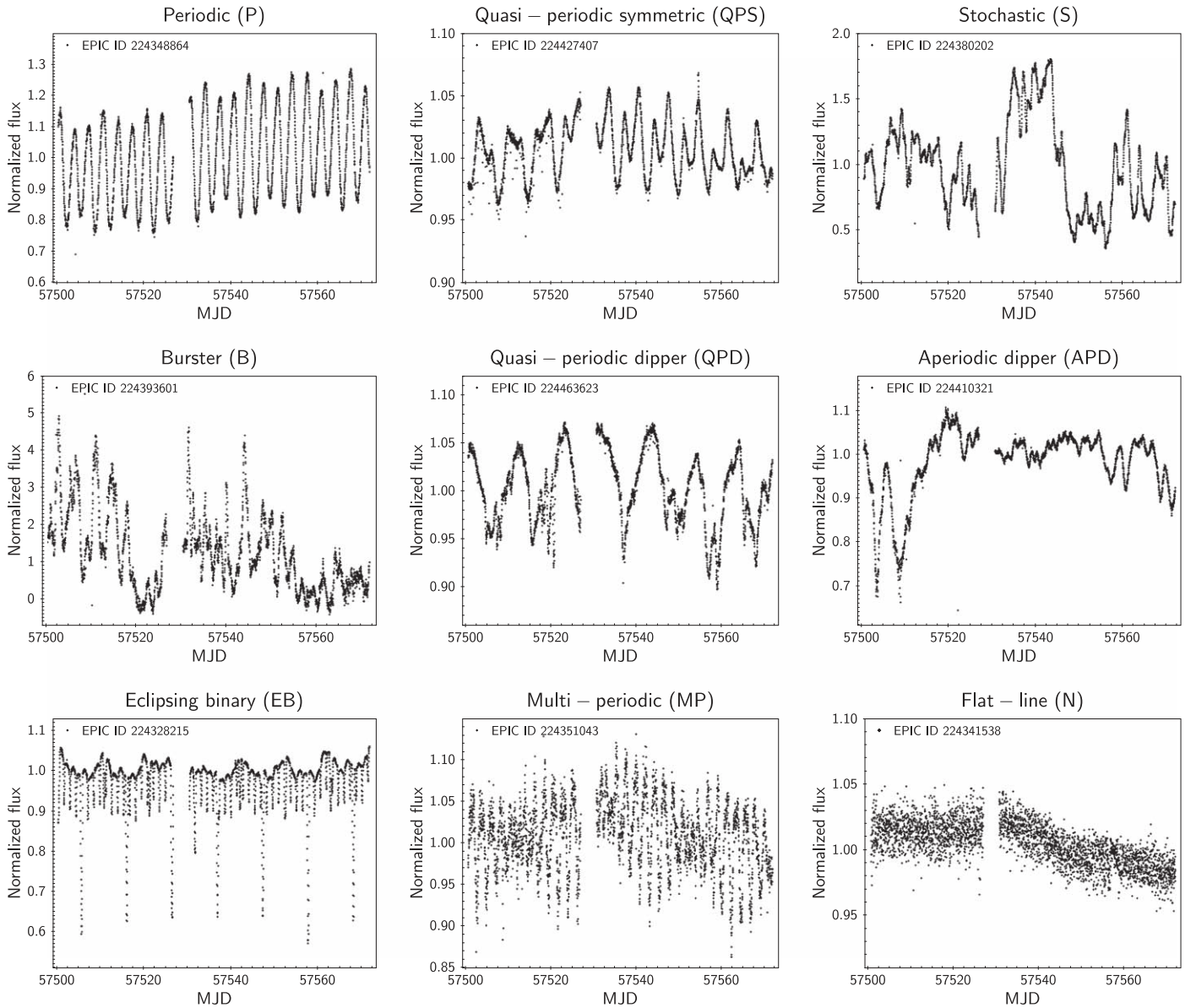


Figure 5. Examples of the different types of variability identified among the K2 light curves of Lagoon Nebula members.

Table 3 summarizes the occurrence rates of each variable class among our sample, as a function of disk status. While disk-bearing sources encompass all categories of variability patterns identified among K2 targets, the most irregular and rapidly varying types of light curves (bursters, stochastic, dippers) are hardly found among disk-free stars, which supports an interpretation of those light-curve patterns in terms of disk-related phenomena. Another inference from Table 3 is that no stars with clear evidence of disks exhibit flat light curves, and very few of them exhibit unclear variability patterns, which indicates that the star–disk activity typically produces well recognizable photometric signatures. Disk candidate stars appear to be an intermediate group of objects between disk-bearing and disk-free sources, with mostly periodic or quasi-periodic variability behaviors, very limited cases of irregular variability, and a significant fraction of cases with unclassifiable variability patterns.

Table 4 summarizes the occurrence rates of different variability behaviors among Lagoon Nebula members of different spectral types. Between 60% and 80% of stars in

each spectral class exhibit periodic, quasi-periodic, or multi-periodic variability patterns. This large fraction of stars with modulated light curves is consistent with earlier results from other CoRoT and Kepler/K2 campaigns, including very young star clusters (e.g., Rebull et al. 2020 on Taurus; Rebull et al. 2018 on ρ Ophiucus and Upper Scorpius; Venuti et al. 2017 on NGC 2264) and somewhat older, nearby clusters (e.g., Rebull et al. 2016 on the ~ 125 Myr old Pleiades; Rebull et al. 2017 on the ~ 790 Myr old Praesepe). We note, however, that other surveys have suggested significantly lower fractions of periodic variables in similarly aged clusters (e.g., Howell et al. 2005, on the ~ 164 Myr old NGC 2301).

Excluding B-type stars (a large fraction of which exhibit unclassifiable variability behaviors, while the remaining majority show regular modulated variability), a few trends can be inferred from Table 4:

1. the fraction of nonvariable stars (which exhibit flat-line light curves) is significantly larger among earlier-type (A, F) stars than among later-type (G, K) stars;

Table 3

Occurrence Rates of Different Light-curve Types (described in Section 4.1) across the Entire Population and as a Function of Disk Status among Lagoon Nebula Members

K2 Class	Total	Disk-bearing	Disk Candidates	Disk-free
P	28.4%	17.4%[15%–21%]	35.8%[31%–41%]	32.4% [30%–35%]
QPS	27.7%	34.9%[31%–39%]	22.6%[19%–27%]	25.2%[23%–28%]
S	6.1%	16.3%[14%–20%]	1.9%[\lesssim 4%]	1.4%[1%–2%]
B	1.8%	5.8%[4%–8%]	–[\lesssim 1%]	–[<1%]
QPD	3.6%	9.3%[7%–12%]	3.8%[3%–6%]	–[<1%]
APD	2.5%	5.8%[4%–8%]	1.9%[\lesssim 4%]	0.7%[\lesssim 1%]
MP	14.4%	5.8%[4%–8%]	15.1%[12%–19%]	19.4%[17%–22%]
EB	2.5%	2.3%[2%–4%]	–[\lesssim 1%]	3.6%[3%–5%]
N	7.2%	–[\lesssim 1%]	5.7%[4%–9%]	12.2%[11%–14%]
U	5.8%	2.3%[2%–4%]	13.2%[10%–17%]	5.0%[4%–6%]

Note. The percentage ranges reported in square brackets correspond to the 1σ confidence intervals ensuing from sample completeness levels in each of the three disk categories. These intervals were estimated by considering the fraction of missing objects and the prevalence of disk-bearing, disk candidate, and disk-free sources as a function of magnitude.

- while a small fraction of stochastic variables are also found among early-type stars, dipping behaviors are only observed among later-type stars;
- multiperiodic variables occur more frequently among earlier-type stars than among later-type stars, while the opposite is true for single-periodicity variables (strictly periodic or quasi-periodic symmetric);
- bursting behaviors appear to be uncommon and concentrated predominantly among higher-mass (A-type, F-type) stars, although the latter inference may be affected by our limited statistics, as discussed in Section 7.1.

4.2. Multiwavelength Correlated Variability from VST/ OmegaCAM Data

To assess the amount of intrinsic variability, beyond the photometric noise level, among Lagoon Nebula members, we implemented the variability index \mathcal{J} defined in Stetson (1996). The \mathcal{J} index measures the amount of correlated variability observed for a given star at two different wavelengths m and m' :

$$\mathcal{J} = \frac{\sum_{k=1}^n w_k \operatorname{sgn}(P_k) \sqrt{|P_k|}}{\sum_{k=1}^n w_k}, \quad (4)$$

where n is the number of time-ordered observations, $P_k = \frac{n}{n-1} \left(\frac{m_k - \bar{m}}{\sigma_m} \right) \left(\frac{m'_k - \bar{m}'}{\sigma_{m'}} \right)$, $\operatorname{sgn}(P_k)$ takes value +1 if P_k is positive and –1 if P_k is negative, m_k and m'_k are the magnitudes measured during the k th observing epoch, \bar{m} and \bar{m}' are the average magnitudes measured across the time series, σ_m and $\sigma_{m'}$ are the photometric uncertainties, and w_k is a weight assigned to each pair of observations m_k and m'_k to take into account, for instance, the exact time lag Δt_k between observations in the k th pair compared to the average Δt measured across all paired observations (e.g., Fruth et al. 2012; Venuti et al. 2015). If the physical drivers of the variability observed at different wavelengths are interconnected, magnitude variations observed simultaneously in different filters are expected to be correlated, yielding a nonzero sum for \mathcal{J} . Conversely, if the photometric fluctuations in the light curve are primarily driven by noise, no correlation is expected between the magnitude variations

measured in different filters, and the \mathcal{J} index will converge to zero.

4.2.1. Implementation of the \mathcal{J} Index Variability Diagnostics

Equation (4) was applied to compute the \mathcal{J} index between simultaneous variations in the u band, r band, and $H\alpha$ band (sensitive to accretion signatures) and between r band and i band (sensitive to photospheric emission and surface spot modulation). Results are illustrated in Figure 6. As expected, field stars are distributed along a narrow sequence close to $\mathcal{J} = 0$, albeit with a small magnitude dependence possibly due to the different levels of photometry accuracy that were attained during long exposures and short exposures to recover the faint and the bright components of the population. A significant dispersion in variability properties is observed among YSO candidates, with a fraction of objects distributed along the sequence of field stars, and another fraction located at larger \mathcal{J} than field stars, which indicates a higher level of intrinsic variability for PMS stars than for main-sequence objects. Class III (disk-free) YSO candidates exhibit an average \mathcal{J} index 10 times larger than that measured for field stars in redder filters (i.e., $\mathcal{J}(r, H\alpha)$ and $\mathcal{J}(r, i)$) and six times larger in the u band (i.e., $\mathcal{J}(u, H\alpha)$ and $\mathcal{J}(u, r)$), affected by larger photometric uncertainties. Class II (disk-bearing) YSO candidates, instead, exhibit average $\mathcal{J}(r, H\alpha)$ and $\mathcal{J}(r, i)$ 40 times larger, and average $\mathcal{J}(u, H\alpha)$ and $\mathcal{J}(u, r) > 20$ times larger, than those measured for field stars.

4.2.2. Statistical Significance of the \mathcal{J} Index Trends

To assess the significance of the distinct trends observed for field stars and YSO candidates in Figure 6, we applied the Energy Test described in Aslan & Zech (2005). Namely, we treated the two-dimensional distributions of the two populations (field stars vs. YSO candidates) on the (mag, \mathcal{J}) diagrams as two systems of charges, one carrying positive charge and the other carrying negative charge. Each individual point in a given system was assigned a charge of magnitude $1/n$, where n is the number of objects in the corresponding distribution, so that each system carries a total charge of unitary magnitude. The test statistic Φ is defined as the sum of three terms: the potential energy of the two systems of charges, Φ' and Φ'' , and the interaction energy between the two systems of charges, Φ^{int} . Each term is defined as follows:

Table 4
Occurrence Rates of Different Variability Types Among Lagoon Nebula Members as a Function of Spectral Class

K2 Class	B Stars (%)		A Stars (%)		F Stars (%)		G Stars (%)		K Stars (%)	
	[16 YSOs]		[30 YSOs]		[17 YSOs]		[39 YSOs]		[124 YSOs]	
P	25.0 ^{+4.4}	[16–38]	16.7 _{-2.0}	[12–24]	22.2 _{-3.2} ^{+4.1}	[16–32]	23.1 _{-2.2} ^{+3.7}	[19–29]	38.1 _{-6.3} ^{+2.4}	[35–42]
QPS	25.0 _{-1.5}	[16–38]	16.7 _{-1.5} ^{+2.7}	[12–24]	11.1 _{-1.6} ^{+4.7}	[8–19]	35.9 _{-4.1} ^{+1.6}	[30–43]	28.6 _{-4.3} ^{+4.2}	[26–32]
S	...	[$\lesssim 6$]	3.3 _{-0.4}	[2–8]	0.0 ^{+5.3}	[$\lesssim 5$]	5.1 _{-0.6} ^{+2.4}	[4–9]	5.6 _{-2.0} ^{+3.6}	[4–7]
B	...	[$\lesssim 6$]	3.3 _{-0.4}	[2–8]	5.6 _{-1.1}	[3–12]	...	[$\lesssim 2$]	0.0 ^{+1.6}	[< 1]
QPD	...	[$\lesssim 6$]	...	[$\lesssim 3$]	...	[$\lesssim 5$]	5.1 _{-0.7}	[4–9]	5.6 _{-1.1} ^{+0.7}	[4–7]
APD	...	[$\lesssim 6$]	...	[$\lesssim 3$]	...	[$\lesssim 5$]	2.6 _{-0.4}	[2–6]	2.4 _{-0.4} ^{+2.3}	[2–4]
MP	12.5 _{-0.7}	[7–23]	30.0 _{-2.7} ^{+2.3}	[23–38]	27.8 _{-5.1}	[20–38]	15.4 _{-2.1}	[12–21]	14.3 _{-2.7} ^{+0.7}	[12–17]
EB	...	[$\lesssim 6$]	3.3 _{-0.4}	[2–8]	5.6 _{-1.1}	[3–12]	2.6 _{-0.4}	[2–6]	0.8 _{-0.2} ^{+0.8}	[$\lesssim 1$]
L	...	[$\lesssim 6$]	...	[$\lesssim 3$]	...	[$\lesssim 5$]	...	[$\lesssim 2$]	...	[< 1]
N	...	[$\lesssim 6$]	20.0 _{-1.8} ^{+2.6}	[14–28]	22.2 _{-3.2} ^{+4.1}	[16–32]	5.1 _{-0.4} ^{+4.7}	[4–9]	1.6 _{-0.3} ^{+1.5}	[1–3]
U	37.5 _{-2.2}	[27–50]	6.7 _{-0.6} ^{+3.0}	[4–12]	5.6 _{-1.1}	[3–12]	5.1 _{-0.7}	[4–9]	3.2 _{-0.6} ^{+1.5}	[3–5]

Note. Uncertainties are estimated from the magnitude distribution of objects in our sample with no SpT estimate and from the magnitude-dependent distribution of different spectral classes in our sample. The ranges given in square brackets correspond to the 1σ confidence intervals calculated by taking into account what fraction of the estimated YSO population per spectral class is included in our sample.

1. $\Phi' = \frac{1}{(n')^2} \sum_{i=1}^{n'} \sum_{j=i+1}^{n'} f(|\mathbf{x}'_i - \mathbf{x}'_j|)$;
2. $\Phi'' = \frac{1}{(n'')^2} \sum_{i=1}^{n''} \sum_{j=i+1}^{n''} f(|\mathbf{x}''_i - \mathbf{x}''_j|)$;
3. $\Phi^{\text{int}} = -\frac{1}{n'n''} \sum_{i=1}^{n'} \sum_{j=1}^{n''} f(|\mathbf{x}'_i - \mathbf{x}''_j|)$.

In the above definitions, $|\mathbf{x}_i - \mathbf{x}_j|$ is the Euclidean distance d between points \mathbf{x}_i and \mathbf{x}_j on the (mag, \mathcal{J}) diagram, and $f(|\mathbf{x}_i - \mathbf{x}_j|)$ is a function of d , defined in Aslan & Zech (2005) as $f(d) = -\ln d$. To prevent the variations along one axis from prevailing numerically over the variations along the other axis, we renormalized all coordinates as $x'_1 = (x_1 - \bar{x}_1)/\sigma_{x_1}$ and $x'_2 = (x_2 - \bar{x}_2)/\sigma_{x_2}$, where x_1 and x_2 are the data point coordinates on the (mag, \mathcal{J}) diagram, \bar{x}_1 and \bar{x}_2 are the average coordinates measured across the sample, and σ_{x_1} and σ_{x_2} are the standard deviations measured around the average coordinates across the sample. For sufficiently large numbers of objects, the total potential energy Φ is expected to reach its minimum value if the two systems of charges are similarly distributed on the plane. Therefore, by measuring how different the measured Φ value is compared to the minimum Φ expectation, we can assess whether the null hypothesis of the two populations being drawn from the same distribution can be rejected to a certain significance.

To build a statistical distribution for the expected minimum Φ under the null hypothesis, we implemented a permutation test as described in Efron & Tibshirani (1993). Namely, we merged the two populations (field stars and YSOs) into a single sample of $n' + n''$ objects. Then, we randomly picked n' objects from the merged sample, with no replacements and no repetitions, to represent the first test population; the remaining n'' objects constituted the second test population. By construction, these two test populations derive from the same statistical distribution, and therefore the Φ statistic measured for them is a realization of the null hypothesis. We repeated this procedure 10,000 times and compared the value of Φ measured for our science populations to the average $\bar{\Phi}$ and its dispersion σ_Φ simulated under the null hypothesis. The test results show clear evidence of a significant difference between the (mag, \mathcal{J}) distribution of field stars and of YSOs when $u + r$, $u + H\alpha$, $r + H\alpha$, and $r + i$ bands are considered. In each of the four cases, no occurrence of Φ larger than that measured for the science samples was obtained after 10,000 permutation

resamples, which indicates that the null hypothesis can be rejected to a p -level $\lesssim 0.0001$.

4.2.3. \mathcal{J} Index versus Spectral Class and K2 Variability

To perform a more quantitative comparison between the variability properties of YSO candidates and field stars, we sorted our sample into magnitude bins and, for each of them, computed the typical \mathcal{J} index for both stellar groups. In order to account for the large scatter in value observed at each magnitude on Figure 6, we applied the bootstrap method and created 100,000 resampled populations for both field stars and YSOs. For each resample, we computed the average $\bar{\mathcal{J}}$ index in each magnitude bin; we then extracted the average $\langle \mathcal{J} \rangle$ as the mean of all $\bar{\mathcal{J}}$ computed in each magnitude bin, while their standard deviation was adopted as the uncertainty associated with the $\langle \mathcal{J} \rangle$ index measurement. Figure 7 illustrates the results of this analysis as a function of magnitude.

Field stars are expected to trace the level of photometric noise across the magnitude range. In all panels of Figure 7, the brightest YSO members (down to \sim early G spectral types) do not exhibit statistical variability above the field population level. Conversely, for fainter magnitudes and later spectral types, the sequence of YSO candidates is clearly distinct from the level traced by field stars, at least down to the faintest objects ($r \geq 19$, well beyond the magnitude limit attained with K2), where photometric uncertainties are considerably larger than for brighter sources (see Figure 2).

As observed in Figures 6 and 7, different levels of variability are statistically associated with different classes of K2 variables. Regular variability patterns (P, QPS, MP, EB) on all diagrams are associated with smaller \mathcal{J} indices than irregular and rapidly evolving variability patterns (B, S, QPD, APD). This trend reflects the fact that B, S, QPD, and APD variables display larger amplitudes of variability (hence larger differences between instantaneous magnitudes and average magnitudes in the \mathcal{J} index definition) than modulated variables. Bursters and aperiodic dippers, in order, exhibit the largest amounts of correlated variability in all diagrams, followed by quasi-periodic dippers and stochastic stars. This progression mirrors the comparative intensities of flux variations that are associated on average with each irregular class,

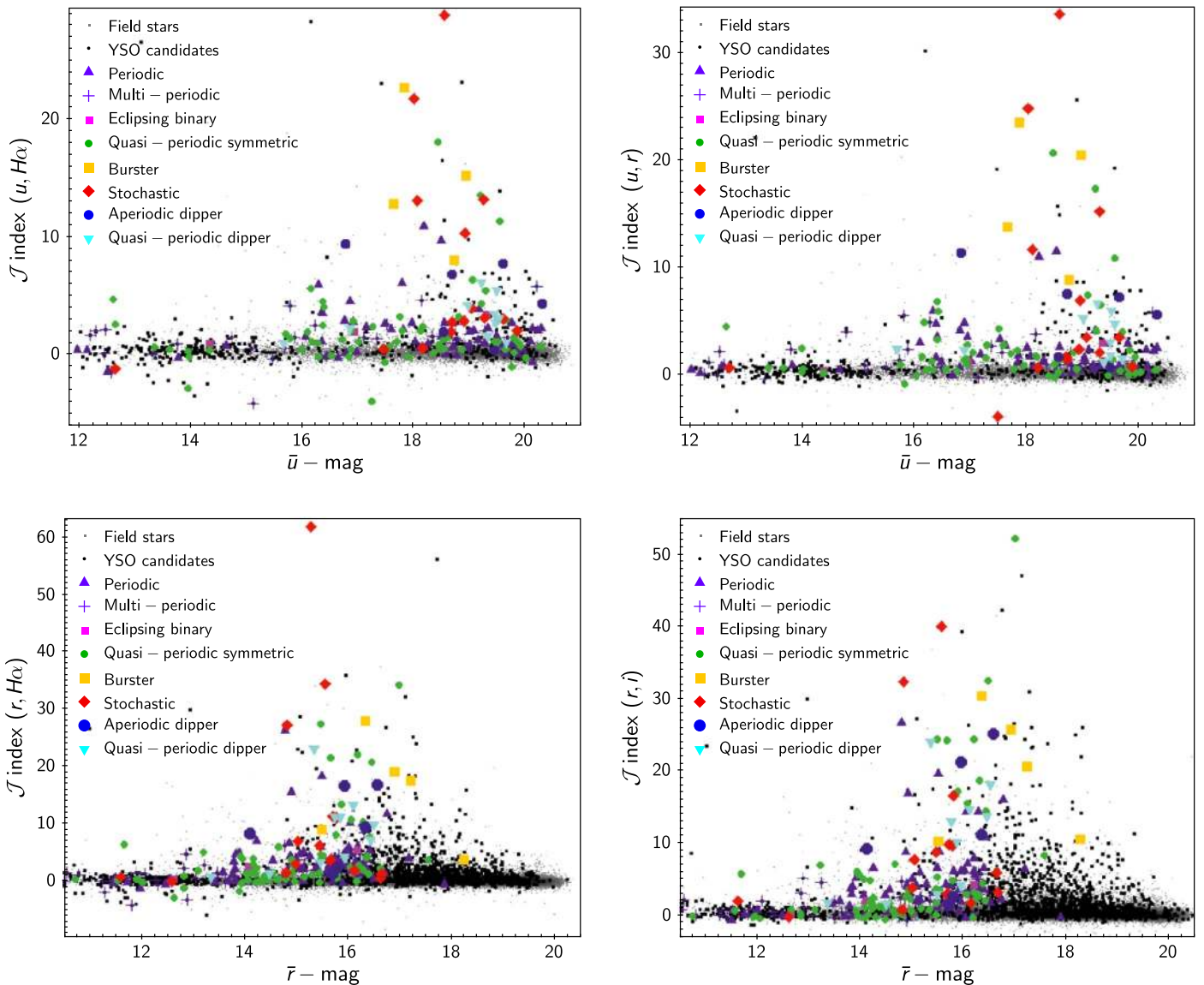


Figure 6. Values of \mathcal{J} index calculated to probe correlated variability in u band and $H\alpha$ band (top left), u band and r band (top right), r band and $H\alpha$ band (bottom left), and r band and i band (bottom right). In each panel, the same color and symbol code are used to distinguish among different stellar groups: field stars (small gray circles), YSO candidates (larger black circles), and various classes of variability identified among K2 targets (P \rightarrow purple upward-pointing triangles, MP \rightarrow purple crosses, EB \rightarrow small fuchsia squares, QPS \rightarrow green filled circles, B \rightarrow large yellow squares, S \rightarrow red diamonds, APD \rightarrow large blue filled circles, QPD \rightarrow cyan downward-pointing triangles). YSOs exhibit on average larger amounts of correlated variability than field stars, and irregular K2 variables exhibit more intense flux variations (translating to higher \mathcal{J}) than regular variables.

both in the K2 time series (see Section 4.1) and in all VST/OmegaCAM filters except the u band, where stochastic variables typically display larger amplitudes of variability than dipper variables. Stochastic stars constitute also the variable class that exhibits the largest case-by-case dispersion in measured \mathcal{J} index, as can be seen in Figure 6.

4.3. Variability Behaviors and Color Properties

In this section we illustrate the color properties of different YSO variables on UV-to-IR photometric diagrams, to identify the leading causes of different variability behaviors, with a particular focus on disk-related phenomena.

4.3.1. Light-curve Morphology and IR Colors

YSO colors at IR wavelengths probe the thermal emission from circumstellar material at different radii from the central

star. Figure 8 illustrates the color properties of Lagoon Nebula members, sorted according to their K2 light-curve morphology, from the J -band ($\sim 1.2 \mu\text{m}$) to $8 \mu\text{m}$ wavelengths. These wavelengths trace reprocessed emission from dust located at distances between $\lesssim 0.1$ au (near-IR) and ~ 5 au (mid-IR) around solar-type stars (Williams & Cieza 2011).

The observed color properties suggest distinct physical origins for regular and irregular variability behaviors. Conspicuous amounts of material in the inner disk regions appear to be characteristic of burster-like, stochastic-like, and dipper-like variables, therefore confirming that these behaviors arise from disk-related phenomena. Modulated behaviors like periodic and quasi-periodic variables, instead, are typically associated with color properties consistent with stellar photospheric emission (e.g., Covey et al. 2007). The typical IR excess emission exhibited by burster stars is larger than, in order, that associated with stochastic stars and dipper stars at

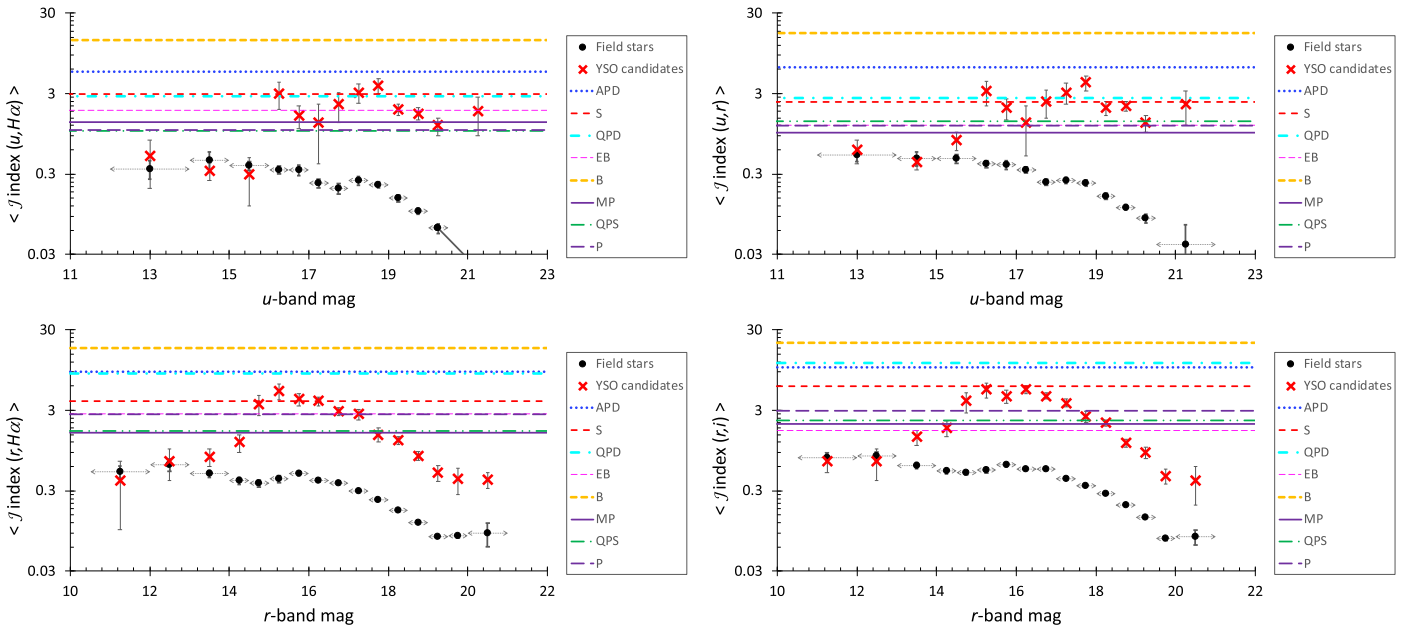


Figure 7. Average values of \mathcal{J} index measured, as a function of u -band magnitude (top) and r -band magnitude (bottom), between u and $H\alpha$ bands (top left), u and r bands (top right), r and $H\alpha$ bands (bottom left), and r and i bands (bottom right). Black circles correspond to the average measurements derived for field stars, and red crosses identify those derived for YSO candidates in the same magnitude bins. The double arrows associated with the field star measurements along the x -axis mark the extent of the magnitude bins in which the average measurements were obtained. $\langle \mathcal{J} \text{ index} \rangle$ estimates, for both the field population and the YSO population, were obtained with the bootstrap method. The associated error bars correspond to the standard deviation of the average \mathcal{J} values measured in each of the 100,000 bootstrap-resampled populations used. Horizontal lines mark the median \mathcal{J} indices computed for different classes of K2 variables, coded in color as in Figure 6, and in dash type as shown in the side legend.

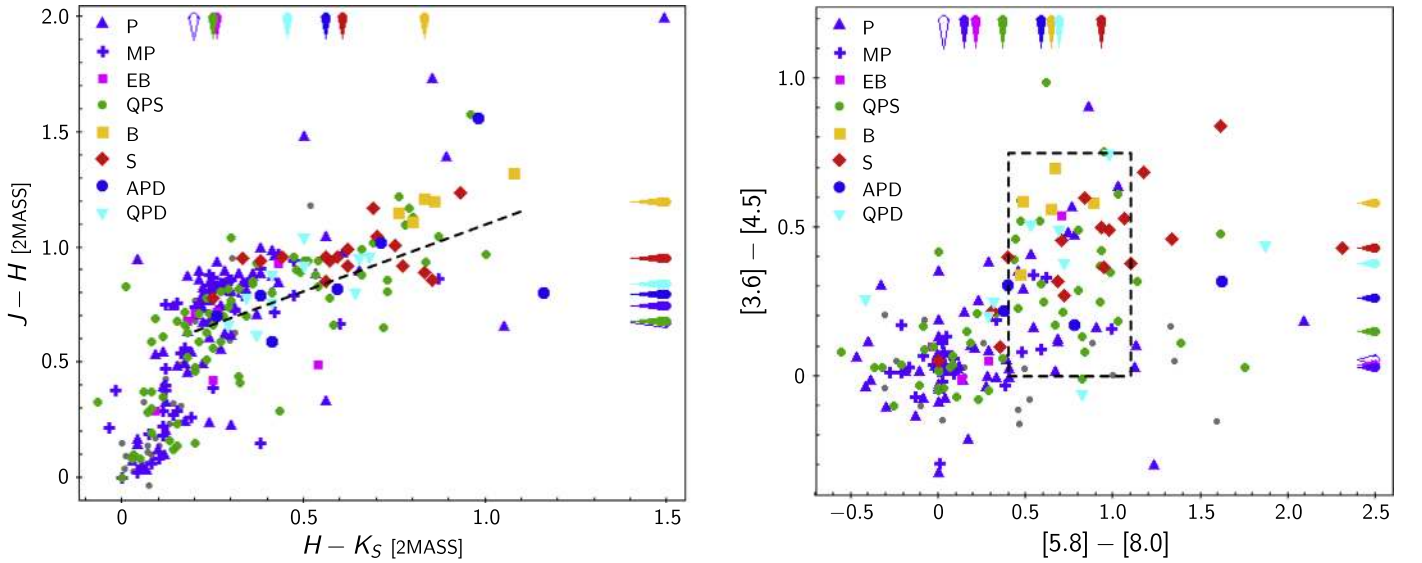


Figure 8. Left: near-IR color properties of K2 Lagoon Nebula members in 2MASS J , H , K_S filters. Different colors and symbols correspond to distinct classes of K2 variables, following the same notation introduced in Figure 6 and summarized in the diagram legend. Markings along the upper and right-hand axes indicate, respectively, the median $H - K_S$ and $J - H$ colors measured for the different variable classes (a filled purple arrow is used to indicate the median colors for P variables, while a contoured arrow is used for MP variables). The color locus for disk-bearing sources defined in Meyer et al. (1997) is traced as a dashed line on the diagram. Right: mid-IR colors measured for K2 Lagoon Nebula members in Spitzer/IRAC filters. Different colors correspond to different variable classes, similarly to what is shown in the left panel. The median colors measured for each class of K2 variables are marked along the upper and right-hand diagram axes. The dashed box indicates the IRAC locus dominated by Class II objects as defined in Allen et al. (2004).

$\sim 1.2\text{--}4.5\ \mu\text{m}$ wavelengths. Stochastic stars, on the other hand, appear to exhibit typically redder $5.8\text{--}8.0\ \mu\text{m}$ colors than bursters and dippers. This may indicate that stochastic variability is driven by time-variable accretion streams that develop beyond the innermost disk regions; however, we do not have sufficient data for our sample from the far-IR Spitzer/Multiband Imaging Photometer (MIPS) or WISE surveys to

assess whether this trend extends to longer ($\sim 20\ \mu\text{m}$) wavelengths.

4.3.2. Light-curve Morphology and UV Photometry

Mass accretion from the inner disk onto the central star is a main ingredient in the dynamics of star-disk interaction in

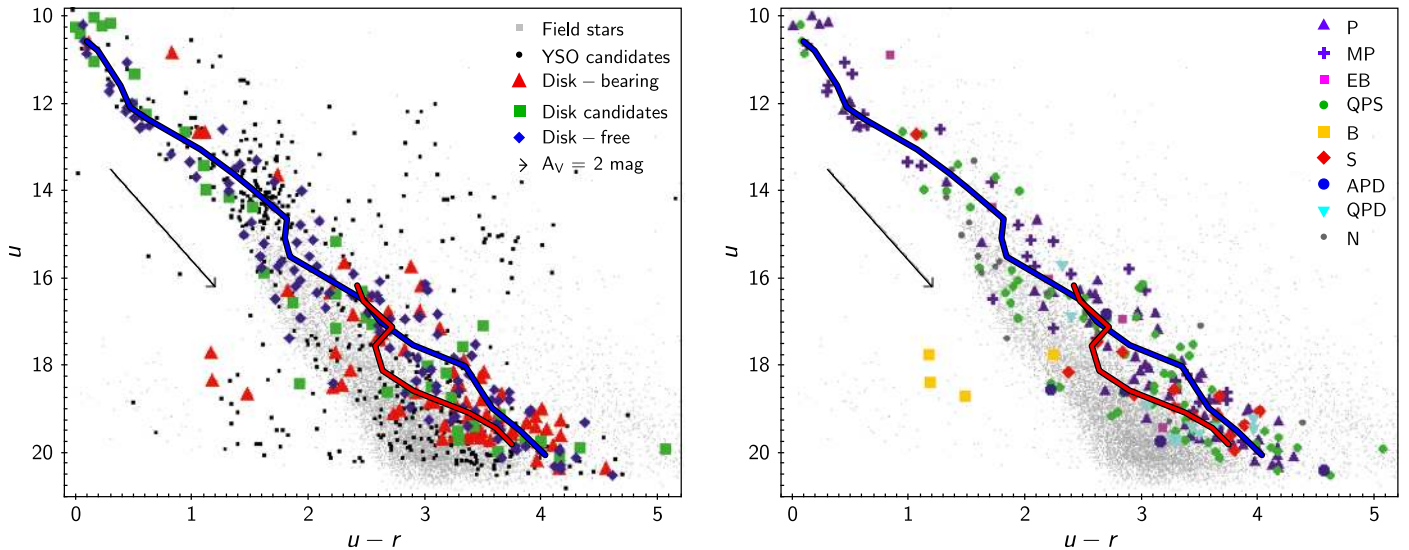


Figure 9. Left: $(u - r, u)$ color-magnitude diagram for stars in the Lagoon Nebula field surveyed with VST/OmegaCAM. Gray circles correspond to field stars, black circles to YSO candidates in the field. Red triangles, green squares, and blue diamonds correspond, respectively, to disk-bearing, disk candidate, and disk-free Lagoon Nebula members monitored with K2. The blue curve and the red curve trace, respectively, the average $u - r$ colors measured as a function of u -band magnitude for disk-free (Class III) and disk-bearing (Class II) objects. The reddening vector on the left of the diagram traces the photometric shift induced by a 2 mag extinction according to a reddening law with $R_V = 5$. Right: same diagram as in the left panel, with K2 Lagoon Nebula YSOs sorted according to their light-curve morphology. Colors and symbols are associated with different variability classes following the same convention as in Figure 6. Nonvariable stars (i.e., flat-line light curves) are indicated as charcoal-gray circles.

YSOs, and UV excess emission represents its most prominent observational signature, as discussed in Section 1. While broadband spectroscopy (e.g., Manara et al. 2013a) provides the most accurate determination of accretion activity above the emission level of the stellar photosphere, U -band (or u -band) photometry has long been shown to be an efficient, reliable proxy to the total accretion luminosity (Gullbring et al. 1998), and it has been used in the literature to map the accretion properties of numerous PMS populations (e.g., Sicilia-Aguilar et al. 2010; Rigliaco et al. 2011; Venuti et al. 2014).

Figure 9 illustrates the $u - r$ colors of young stars in the Lagoon Nebula in relation to their u -band magnitudes. Confirmed cluster members monitored with K2 form a distinct, albeit scattered, sequence, located above the distribution of field stars (i.e., at brighter magnitudes) at any given $u - r$ interval. While the distributions of disk-bearing and disk-free stars are largely overlapping (Figure 9, left panel), we did ascertain distinct trends in the average $u - r$ colors measured for disk-free and disk-bearing stars as a function of u -mag. Namely, we calculated a moving average of the observed $u - r$ for different YSO groups by sampling the u -magnitude range in 1 mag wide bins with a step of 0.5 mag. The derived average trends of u versus $u - r$ for disk-free and disk-bearing objects are shown, respectively, as a blue curve and a red curve in Figure 9 (left). The average $u - r$ measured for disk-free stars in a given u -mag bin tends to be larger than that measured, in the same magnitude range, for disk-bearing stars at $u \gtrsim 17.5$, where Class II YSOs are most represented. Disk candidate YSOs, as classified in Section 3.2, follow a similar color distribution to that of disk-bearing YSOs, as the majority of them lie to the left of the average sequence for disk-free stars (i.e., at lower $u - r$ values). The lower-on-average $u - r$ colors measured for disk-bearing and potential disk-bearing objects, as opposed to disk-free objects, suggest that many of these sources exhibit some excess emission in the u band, indicative of ongoing accretion activity.

The right panel of Figure 9 shows how different types of K2 variables compare in terms of their $u - r$ properties. Strictly periodic variables tend to follow closely the average $(u - r, u)$ sequence of disk-free stars, as also observed for quasi-periodic variables, albeit with a larger scatter around the average sequence. This suggests that a modulated variability behavior is driven primarily by photospheric features. Dipper stars, on the other hand, tend to be located to the left of the average disk-free color sequence, and burster stars tend to exhibit $u - r$ color excesses significantly larger than the average measured for typical disk-bearing YSOs. This result confirms previous findings that a bursting behavior is associated with high accretion levels (Stauffer et al. 2014; Venuti et al. 2014; Cody et al. 2017). Stochastic stars also appear to be primarily located at bluer colors than the average photospheric behavior, but, contrary to burster stars, they do not stand out with respect to other disk-bearing objects.

4.3.3. Light-curve Morphology and $H\alpha$ Photometry

$H\alpha$ line emission is another widely used indicator of ongoing disk accretion onto young stars. $H\alpha$ emission is thought to be produced by the heated gas in the magnetospheric accretion flows; therefore, UV excess emission and $H\alpha$ emission probe two distinct, albeit interconnected, components of the magnetospheric accretion process. Several studies have shown a definite correlation between the continuum excess emission of accreting YSO populations and their $H\alpha$ luminosity, measured simultaneously (e.g., Alcalá et al. 2014, 2017). The $H\alpha$ luminosity is therefore considered a reliable statistical diagnostic of the presence of accretion, although quantitative measurements of the amount of accretion on individual sources can vary depending on the indicator used (e.g., Antonucci et al. 2011; Manara et al. 2013b). As spectroscopic surveys of $H\alpha$ emission can be time-consuming and are often restricted to small and/or nearby YSO populations, photometric surveys in narrowband $H\alpha$ filters, combined with other optical filters (e.g., V, r, i), represent an efficient alternative

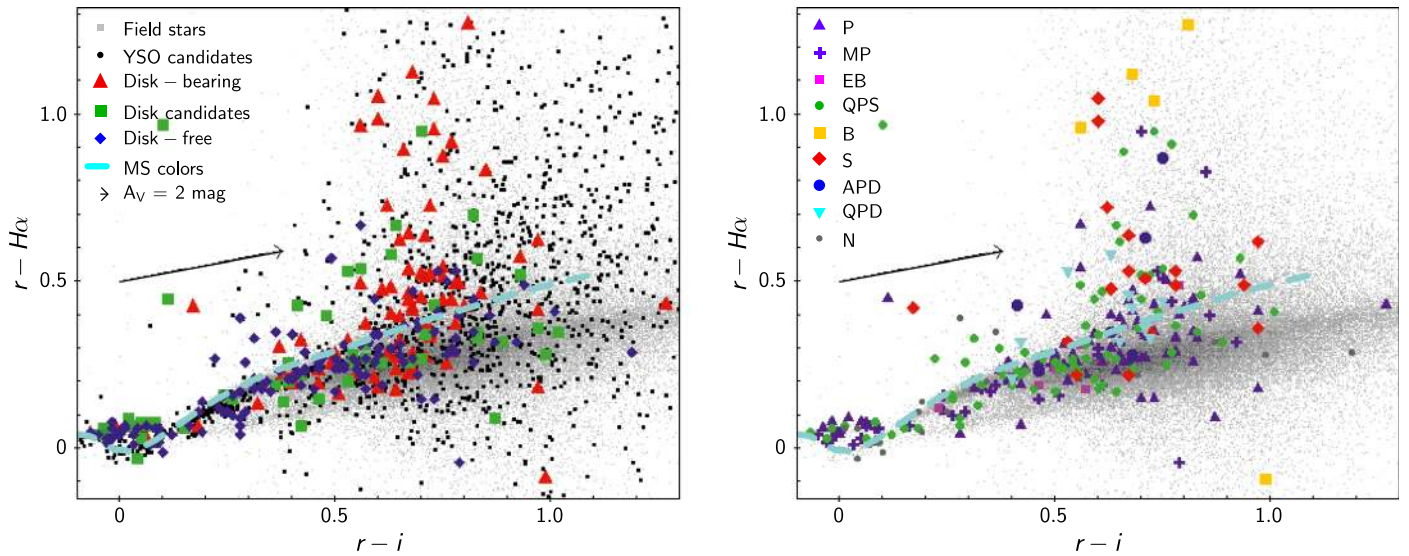


Figure 10. Left: $(r-i, r-H\alpha)$ color properties of field stars (gray circles) and YSO candidates (black circles) in the Lagoon Nebula region from VST/OmegaCAM photometry. Synthetic colors for main-sequence stars in the same filters, as tabulated by Drew et al. (2014), are dashed in cyan to guide the eye. Lagoon Nebula members monitored with K2 and classified as disk-bearing, disk-free, or disk candidates (see Section 3.2) are marked further as red triangles, blue diamonds, and green squares, respectively. The effect of reddening is illustrated as a black vector with $A_V = 2$ mag. Right: $r, i, H\alpha$ color distribution of K2 Lagoon Nebula members, sorted according to their light-curve morphology (see Section 4.1). The color and symbol convention for each class is the same as adopted for Figure 6. Nonvariable stars (i.e., those that exhibit flat-line light curves) are shown as large charcoal-gray circles. Disk-bearing stars and irregular K2 variables are shown to exhibit on average higher levels of $H\alpha$ emission (translating to larger $r-H\alpha$ colors) than can be accounted for by photospheric and chromospheric activity.

to provide a statistical map of accretion activity in large cluster populations (e.g., De Marchi et al. 2010; Barentsen et al. 2011, 2014; Biazzo et al. 2019).

Figure 10 illustrates the color properties of field stars and Lagoon Nebula YSOs on the $(r-i, r-H\alpha)$ diagram. As already observed for the u -band properties in Figure 9, the color loci occupied by disk-bearing and disk-free stars overlap significantly (left panel). However, their distributions exhibit statistical differences, as 56% of disk-bearing YSOs have $r-H\alpha$ colors above the photospheric level for main-sequence dwarfs (i.e., they exhibit an enhanced emission at $H\alpha$ wavelengths), while this percentage is only 27% among disk-free members and 36% among disk candidate YSOs.¹⁰ Burster stars exhibit the largest $r-H\alpha$ colors (right panel), followed by stochastic stars; in both categories, an excess in $H\alpha$ emission with respect to the photospheric level is detected for $\sim 80\%$ of the objects. About two-thirds of the dipper stars also exhibit redder $r-H\alpha$ colors than the main-sequence level. The percentage of YSOs with enhanced $H\alpha$ emission is instead lower among quasi-periodic variables ($\sim 40\%$) and strictly periodic sources ($\sim 30\%$).

5. Correlated Color–Luminosity Variability

Multiwavelength variability and color monitoring provide key information on the physical drivers of the observed YSO behavior. Indeed, while disk-related phenomena typically induce larger magnitude variations than stable photospheric activity (dark starspots; e.g., Vrba et al. 1993; Bouvier et al. 1995; Grankin et al. 2008; Venuti et al. 2015), it is the associated color variability that enables discriminating between different physical scenarios. Luminosity modulation by surface features, be them cold magnetic spots or hot accretion shocks, always produces larger

variability amplitudes at shorter wavelengths; it is the rate at which the amplitudes decrease toward longer wavelengths that allows us to constrain the physical conditions of the modulating features. Similarly, monitoring the time variability of $u-r$ and $r-H\alpha$ colors (indicative of accretion activity) as the stellar flux evolves provides details on the accretion geometry in disk-dominated YSO variables.

To probe the comparative nature of flux variations in disk-dominated YSOs that belong to distinct K2 morphology classes, we investigated the simultaneous K2 flux and VST/OmegaCAM $u, r, H\alpha$ color variations for Lagoon Nebula objects in our sample that were detected in all filters and exhibit either a burster, a stochastic, or a dipper light curve. As reported in Sections 2.2 and 2.3, our VST survey of the Lagoon Nebula overlapped with the last 2 weeks of the K2 run, and roughly two-thirds of the VST observing epochs were acquired during this time window. For each object, we cross-correlated the K2 light curves with the VST color time series and retained those epochs that match in time within an interval of 0.01 days (i.e., < 15 minutes), in order to avoid erroneous flux and color associations for short-lived variability phenomena (e.g., bursts with duration of hours; see Stauffer et al. 2014; Cody et al. 2017). Examples of how color variations are associated with luminosity variations across our sample are reported in Figure 11. To investigate any trends between flux variations and color variations, we measured the degree of correlation between simultaneous K2 flux measurements and, in turn, $u-r$ and $r-H\alpha$ colors. We applied a simple least-squares fit model to derive the slope of the best correlation trend and then evaluated its significance against the average slope and slope dispersion (σ) obtained for 100 randomly shuffled and recombined sets of the original flux and color measurements for the object. We retained as significant those correlation or anticorrelation trends whose slope stood at least 1σ away from the average slope derived from the 100 simulated sets. The statistical results of this analysis are reported in Table 5.

¹⁰ Objects with $r-i < 0.25$ and $r-H\alpha < 0.2$ were not considered for this computation, since their location above the main-sequence track may be caused by nonzero extinction, and dereddening their photometry would render their colors consistent with the main-sequence level.

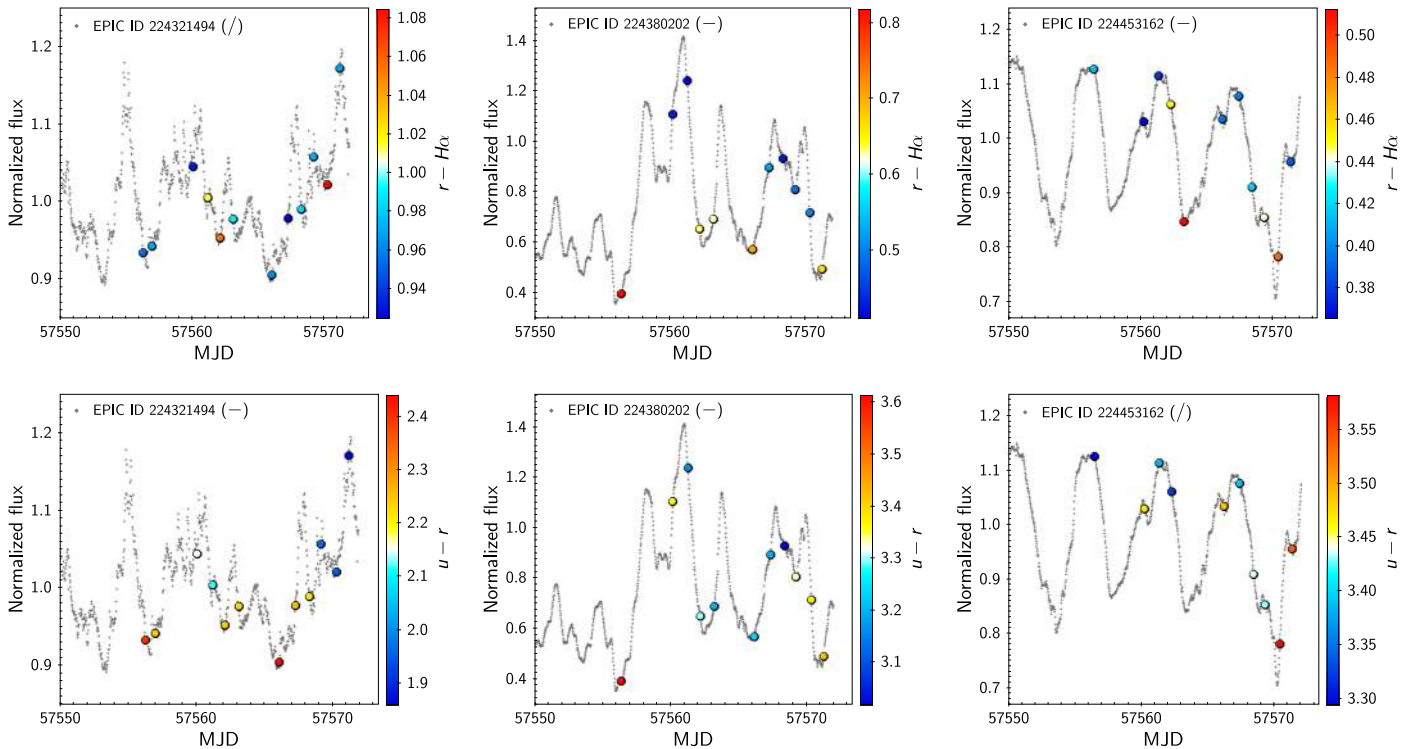


Figure 11. Last 25 days of the K2 light curves for selected Lagoon Nebula YSOs, representative of the burster (left panels), stochastic (middle panels), and quasi-periodic dipper (right panels) variable classes, with superimposed measurements of the instantaneous $r - H\alpha$ (top panels) and $u - r$ (bottom panels) colors, obtained simultaneously with VST/OmegaCAM. The range of color values is matched to a color scale, as indicated to the right of each panel. The state of correlation between flux variations and color variations, tested as described in the text, is indicated in each panel next to the target’s EPIC ID, following the convention adopted in Table 5 (+ for positive correlation trends, – for negative correlation trends, and / for noncorrelated trends).

A first clear indication from this analysis is that very few objects with disk-dominated variability exhibit a positive correlation between their flux and their $u - r$ colors. This implies that brighter states for these sources typically correspond to enhancements of their u -band luminosity (leading to lower, hence bluer, $u - r$ values). An anticorrelation trend between flux and $u - r$ measurements is detected in all burster stars in our sample and in two-thirds of the stochastic stars. This is consistent with our interpretation that the most prominent flux variations exhibited by these sources are associated with discrete accretion events and the resulting shock emission. A definite correlation or anticorrelation trend with $r - H\alpha$ is detected in a smaller number of cases for these two classes, 75% of our small sample of bursters, and around 50% of our stochastic stars. This is also consistent with the fact that the $H\alpha$ emission provides a more indirect proxy for accretion onto the star than UV emission, and it originates from a more extended region in the inner disk environment. All of the burster stars for which a definite flux versus $r - H\alpha$ trend is found (75%) exhibit an anticorrelation between these two quantities, which suggests that the peaks in brightness for these objects correspond to phases of unobstructed view onto the accretion shock regions, when continuum emission is enhanced with respect to the measured line emission (yielding smaller $r - H\alpha$ values). Conversely, one-third (33.3%) of the stochastic stars exhibit a positive correlation between their flux and $r - H\alpha$ values, 2.5 times more numerous than those (13.4%) that instead exhibit an anticorrelation trend. This suggests a geometry where, at the brightness peak or close to it, both surface accretion features (shocks) and extended accretion funnels are visible. The accretion dynamics in burster stars is believed to be governed by instabilities at the interface between the stellar magnetosphere

and the inner disk rim; such instabilities prevent the formation of magnetospheric-driven accretion columns and instead fuel accretion onto the star via thin, equatorial tongues of material that are only funneled along the magnetic field lines when they are already close to the stellar surface (Kulkarni & Romanova 2008). A somewhat different accretion mechanism was proposed for stochastic stars (Stauffer et al. 2016), namely, a variable influx of material feeds into magnetically channeled accretion flows, which translates to stochastically variable mass loads onto the star, and to rapidly evolving hot spot regions. This picture would link stochastic stars to aperiodic dippers seen at lower inclinations and is consistent with the differing color trends we observe, on a statistical level, between burster stars and stochastic stars.

Among dipper stars, only around half of the aperiodic dippers, and 30% of the quasi-periodic dippers, exhibit a definite anticorrelation trend between their flux and $u - r$ variations. The decrease in detection of anticorrelated f_{norm} versus $u - r$ trends from B to QPD variables in Table 5 may suggest that stochastic stars and aperiodic dippers represent an intermediate mode of star-disk interaction between the instability-driven regime observed in bursters and the stable funnel-flow regime observed in quasi-periodic variables. About a third of aperiodic dippers and the majority of quasi-periodic dippers exhibit no specific trend in $u - r$ as their luminosity varies. This may be a consequence of the fact that, in dipper stars, the most prominent flux variations (recurring luminosity dips) are a product of variable extinction by clumps of material in the inner disk environment, which can effectively mask the luminosity variations induced by accretion shocks. Around 45% of dipper stars exhibit a definite trend between their flux variations and their $r - H\alpha$ behaviors; among these, the most common behavior is an

Table 5

Statistics on the Fractions of Disk-bearing Lagoon Nebula YSOs, with K2 Light Curves Classified as Burster (B), Stochastic (S), Aperiodic Dipper (APD), Quasi-Periodic Dipper (QPD), or Quasi-periodic Symmetric (QPS), that Exhibit Correlated (+), Anticorrelated (-), or Noncorrelated (/) Trends between Their K2 Normalized Light-curve Flux (f_{norm}) and the $u-r$ and $r-H\alpha$ Color Variations Monitored with VST/OmegaCam

f_{norm} Trend	B [4 YSOs]	S [15 YSOs]	APD [6 YSOs]	QPD [10 YSOs]	QPS [25 YSOs]
$\propto \begin{matrix} + (u-r) \\ + (r-H\alpha) \end{matrix}$
$\propto \begin{matrix} + (u-r) \\ - (r-H\alpha) \end{matrix}$	8.0%
$\propto \begin{matrix} - (u-r) \\ + (r-H\alpha) \end{matrix}$...	20.0%	4.0%
$\propto \begin{matrix} - (u-r) \\ - (r-H\alpha) \end{matrix}$	75.0%	6.7%	33.3%	...	8.0%
$\propto \begin{matrix} \pm(u-r) \\ + (r-H\alpha) \end{matrix}$...	13.3%	16.7%	...	8.0%
$\propto \begin{matrix} \pm(u-r) \\ - (r-H\alpha) \end{matrix}$...	6.7%	...	40.0%	16.0%
$\propto \begin{matrix} + (u-r) \\ \pm(r-H\alpha) \end{matrix}$...	6.7%	16.7%	...	12%
$\propto \begin{matrix} - (u-r) \\ \pm(r-H\alpha) \end{matrix}$	25.0%	40.0%	16.7%	30.0%	20%
$\propto \begin{matrix} \pm(u-r) \\ \pm(r-H\alpha) \end{matrix}$...	6.7%	16.7%	30.0%	24%

Note. The number of YSOs, in each light-curve category, for which the flux-color trend could be analyzed is reported below each category label in the table header. Rows shaded in gray correspond to an anticorrelation trend between f_{norm} and $u-r$, expected in the case of accretion-dominated variability.

anticorrelation trend, which indicates that their $r-H\alpha$ is largest at their lowest luminosity levels (i.e., inside the dips). Larger values of $r-H\alpha$ correspond to an enhancement of the narrowband $H\alpha$ emission with respect to the r -band continuum emission. This trend is qualitatively consistent with a scenario in which flux dips are produced by an inner disk warp at the base of a magnetospheric accretion column, where the phase of minimum photospheric visibility coincides with a maximum in accretion funnel visibility. The large number of dipper variables for which no specific trends between flux variations and color variations were found may be explained in terms of multiple coexisting accretion streams or columns, and/or assuming a delayed appearance of accretion features and occultation features. The latter may be a common scenario, as suggested by earlier studies (McGinnis et al. 2015) where direct evidence of hot spots appearing simultaneously with the main occultation event was recovered only in a minority of cases.

A redder spectrum at lower luminosity states is also expected for stars with variability dominated by surface spot modulation, as mentioned earlier. Indeed, for spots hotter than the photosphere, the spot spectrum peaks at shorter wavelengths than the stellar spectrum, resulting in an enhanced spot-to-photosphere contrast at bluer wavelengths. Conversely, for spots colder than the photosphere, the spot spectrum peaks at longer wavelengths than the stellar spectrum, resulting again in an enhanced spot-to-photosphere contrast at bluer wavelengths. However, when both cold and hot spots are present at the stellar surface (as is likely for quasi-periodic symmetric variables in our sample), we may expect their photometric signatures to overlap and mask any color correlation. Indeed, as

reported in Table 5, quasi-periodic symmetric stars are found to exhibit a wide range of color behaviors. Only about a third of YSOs in this category, among our disk-bearing stars, exhibit a clear anticorrelation trend between the K2 flux intensity and the VST $u-r$ color; this percentage is similar to what is observed among quasi-periodic dippers. Conversely, about half of the quasi-periodic symmetric variables do not exhibit a definite correlation trend with $u-r$ and/or $r-H\alpha$ colors.

6. Timescales of Variability from K2 Light Curves

In order to probe the characteristic timescales of variability of Lagoon Nebula members, irrespective of the periodic or aperiodic nature of their variation patterns, we adopted the method of structure functions (Simonetti et al. 1985; Hughes et al. 1992; de Vries et al. 2003), as recently implemented to study YSO variability by Sergison et al. (2020). The method consists of extracting every timescale of variability τ encompassed by the time series and, for each τ , computing the average amplitude of normalized flux variability among all pairs of points in the light curve that are spaced by that time interval τ . The structure function (\mathcal{SF}) is then defined as the average variability amplitude measured within the light curve as a function of τ . In order to apply the \mathcal{SF} method to a discrete time series, with possibly unevenly spaced data, we first identify the range of investigated τ , from τ_{min} (i.e., the minimum timescale of variability that can be reliably extracted from the light curve) to τ_{max} (i.e., the maximum timescale of variability that can be reliably extracted from the light curve). We then divide this ($\tau_{\text{min}}, \tau_{\text{max}}$) range into logarithmically spaced timescale bins, and, for each bin (τ_1, τ_2), we select all

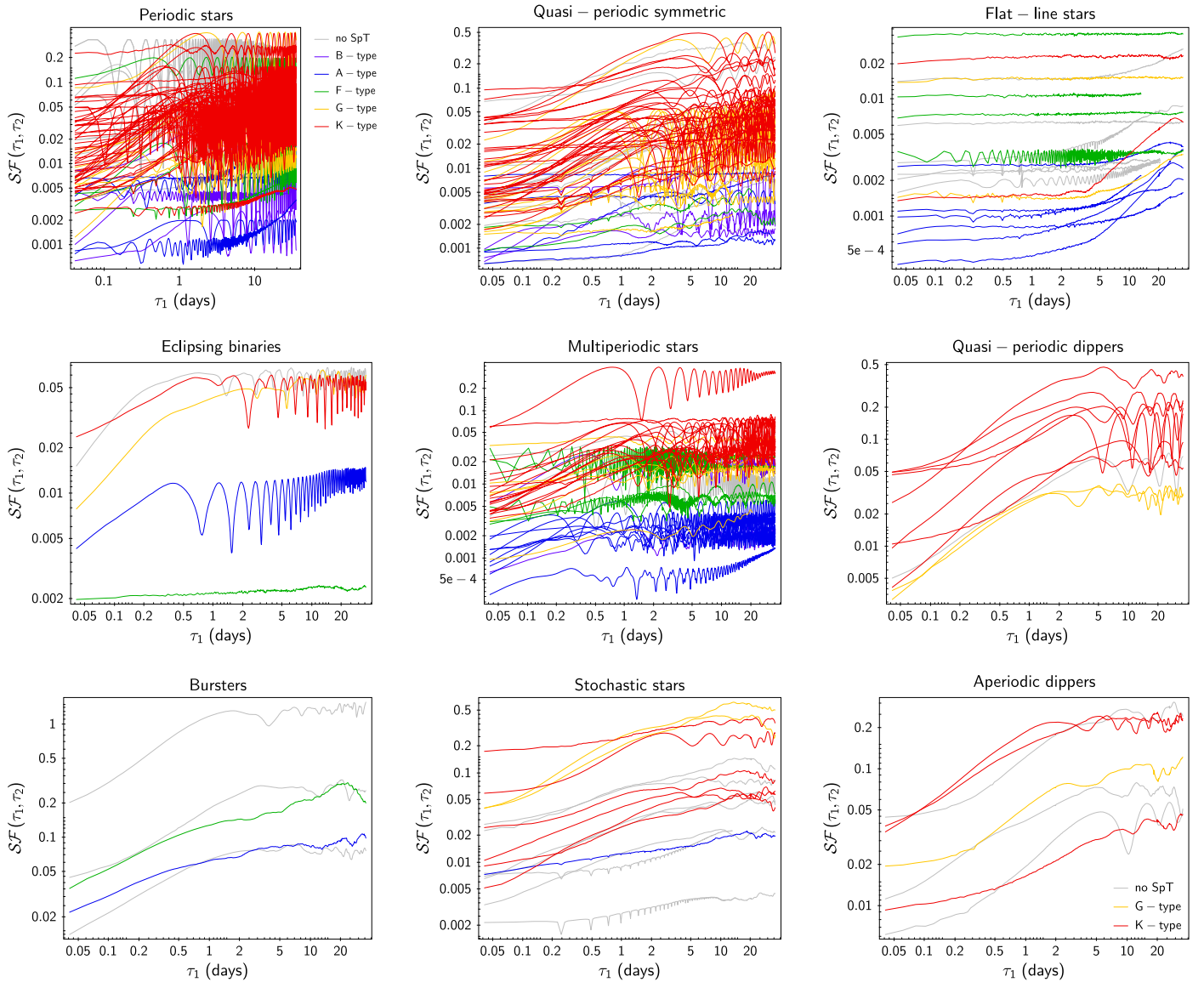


Figure 12. Structure functions \mathcal{SF} computed for each K2 light curve on timescales τ ranging from twice the data cadence to half the light-curve span, sampled as discussed in Section 6. For each bin (τ_1, τ_2) of investigated variability timescales, the value of \mathcal{SF} resulting from Equation (5) is plotted as a function of τ_1 for illustration purposes. Each class of light-curve variability is shown in a different panel, as indicated on top of each diagram (the “U” class described in Section 4.1 is not included here). Different colors identify different SpT, as detailed to the right of the top left panel (purple \rightarrow B-type stars; blue \rightarrow A-type stars; green \rightarrow F-type stars; yellow \rightarrow G-type stars; red \rightarrow K-type stars; gray \rightarrow stars with no SpT estimate from the procedure in Section 3.1). On all panels, it is possible to observe a systematic increase of the intrinsic variability amplitude (as traced by the value of \mathcal{SF} in the plateau region at large timescales) from earlier-type stars to later-type stars.

pairs of light-curve epochs (t_i, t_j) , where $j > i$ and $\tau_1 < t_j - t_i < \tau_2$. The average variation in normalized flux, measured across all pairs of selected points, defines the value of $\mathcal{SF}(\tau_1, \tau_2)$ as

$$\mathcal{SF}(\tau_1, \tau_2) = \sqrt{\frac{1}{N(\tau_1, \tau_2)} \sum_{j>i} (f_i - f_j)^2}, \quad (5)$$

where $N(\tau_1, \tau_2)$ is the number of pairs of light-curve points (i, j) separated in time by an amount between τ_1 and τ_2 , and f_i is the normalized flux measured at time t_i .

From a theoretical standpoint, the behavior of $\mathcal{SF}(\tau)$ is expected to consist of three main separate regimes (see Figure 7 of Sergison et al. 2020). Initially, the \mathcal{SF} is expected to be relatively flat or slowly increasing with τ , corresponding to the short- τ regime where the observed flux variations are dominated by photometric uncertainties rather than intrinsic

variability. In a second phase, the \mathcal{SF} starts rising above the noise-dominated level and increases as a power law, with a specific gradient that reflects the nature of the observed variability. The power-law rise continues until a limiting value τ_{high} , which corresponds to the largest timescale at which intrinsic variability is observed along the time series (i.e., the variability observed beyond τ_{high} merely reflects the variability displayed on shorter timescales). $\mathcal{SF}(\tau > \tau_{\text{high}})$ therefore exhibits a newly flat or slowly varying trend around the value of $\mathcal{SF}(\tau_{\text{high}})$. We selected our τ_{min} to correspond to twice the light-curve cadence (i.e., $\tau_{\text{min}} \sim 0.04$ d), and our τ_{max} as half the total light-curve span (i.e., $\tau_{\text{max}} \sim 35.5$ d). We then sampled this interval in 1000 equal bins in logarithmic space, and for each bin we computed the value of \mathcal{SF} as defined in Equation (5). The resulting $\mathcal{SF}(\tau)$ are illustrated in Figure 12 for different light-curve behaviors and spectral classes.

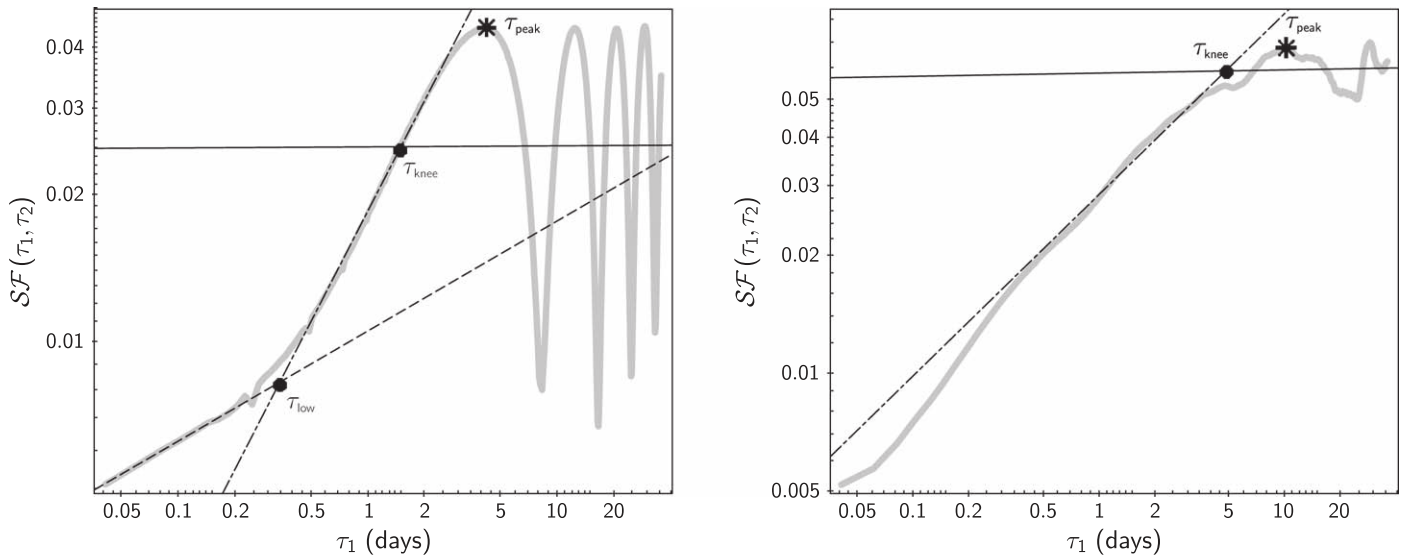


Figure 13. Examples of \mathcal{SF} analysis conducted on K2 light curves to extract the characteristic timescales of variability. The \mathcal{SF} shown in gray on the left belongs to the K-type star EPIC ID 224438171, whose variability behavior is classified as P, while the one shown on the right belongs to the K-type star EPIC ID 224337699, classified as S. The dashed black line traces the best power-law fit derived for the first \mathcal{SF} regime (τ range where the photometric noise is predominant; not observed in the second case). The dashed-dotted black line traces the best power-law fit derived for the main \mathcal{SF} regime (τ range dominated by intrinsic variability on the corresponding timescales). The solid black line traces the best power-law fit to the third \mathcal{SF} regime (τ range where the observed variability is a reflection of the variability observed on shorter timescales). The timescales of intersection between first-regime and second-regime fits (τ_{low}) and between second-regime and third-regime fits (τ_{knee}) are marked as large black circles. The asterisk marks the timescale corresponding to the first observed maximum in the \mathcal{SF} (τ_{peak}). The small negative spikes, visible in the \mathcal{SF} on the left at $\tau \sim 0.24$ days, 0.49 days, and repeatedly after that, are spurious features induced by the corrective thruster firings operated roughly every 6 hr during the K2 mission (Howell et al. 2014).

As already discussed in Section 4.2, later-type stars (shown in yellow and in red in Figure 12) tend to exhibit systematically higher amounts of variability than earlier-type stars (purple and blue). Flat-line (or nonvariable) stars (Figure 12, top right panel) exhibit either an overall constant \mathcal{SF} throughout the τ range or an initially flat trend (up to timescales of a few days) that subsequently increases exponentially with τ until the end of the timescale domain. This indicates that the flux variations observed for light curves classified as “N” are dominated either by luminosity fluctuations that appear with similar amplitudes throughout the monitored span or by light-curve systematics that impact the observed amplitude of luminosity variations as the considered time span increases. In the other light-curve categories, two or three distinct regimes are typically identified in the observed \mathcal{SF} , which correspond to the τ domains dominated respectively by photometric noise, intrinsic variability, and reflected variability from shorter timescales.

To investigate the nature and characteristic timescales of variability of each class, we fitted a power law ($\mathcal{SF} \sim k\tau^\beta$) to each distinct segment of \mathcal{SF} for each object, as illustrated in Figure 13. We then extracted the coordinates of the intersection points between the separate fits (which correspond to the approximate timescales, τ_{low} and τ_{knee} , where the transition from one \mathcal{SF} regime to the next occurs). These two timescales of intersection delimit the approximate range of timescales within which intrinsic variability is observed. The oscillations observed beyond τ_{knee} reflect the periodicity of the observed variability (a maximum in \mathcal{SF} is measured when the pairs of data points separated by the corresponding timescale are collected at opposite variability phases, while a minimum in \mathcal{SF} is measured when the timescale considered is a multiple of the actual variability period in the light curve). We also extracted the location of the first observed peak in the \mathcal{SF} , as well as the slope of the fit to the intrinsic variability-dominated regime, which holds clues to the origin of the observed

variability. A clear three-component fit, with the identification of a τ -region dominated by photometric noise, was obtained in $\sim 60\%$ of the cases. Many of the cases where no noise-dominated region could be identified in the \mathcal{SF} (i.e., where intrinsic variability is observed already at the shortest investigated τ) correspond to stars where the maximum timescale of intrinsic variability is comparatively short: over 65% of stars where the first \mathcal{SF} peak is located at $\tau_{\text{peak}} < 1$ day exhibit no noise-dominated regime, while among stars with $\tau_{\text{peak}} \geq 1$ day this percentage is only 16%. The fraction of stars whose \mathcal{SF} is initially dominated by photometric noise is especially low among multiperiodic stars or eclipsing binaries, possibly due to the coexistence of multiple cyclic variability trends. Another category with no substantial noise-dominated τ -region is that of burster stars, which exhibit the most intense, and often short-lived, flux variations (e.g., Cody et al. 2017). For the other categories of stars, the median τ_{low} measured ranges from ~ 0.2 to ~ 0.4 days and tends to be higher among irregular variables than among regular variables.

The index β of the best power-law fit to the \mathcal{SF} region dominated by intrinsic variability can vary broadly from case to case: measured values for our K2 sample of Lagoon Nebula members span the entire range from < 0.1 to 0.9. As discussed in Sergison et al. (2020),¹¹ a $\beta \sim 0$ value is expected in the case of a light curve dominated by uncorrelated (white) noise, such as those of stars labeled as “N” in the K2 sample (Section 4.1). Indeed, all of our targets in this class with a power-law fit solution to their \mathcal{SF} have $0 \leq \beta < 0.05$. A power-law index $\beta \simeq 0.05$ describes an \mathcal{SF} dominated by flicker-noise

¹¹ The definition of the \mathcal{SF} we adopt here (Equation (5)) is the square root of the definition adopted by Sergison et al. (2020, Equation (2)). Therefore, the reference values for the power-law index β discussed in their Table 6 are double the values that need to be considered here for comparison with our fit parameters.

variability (Press 1978), characterized by an overall underlying trend of larger variability amplitudes for longer timescales (which can exhibit superimposed, shorter-term coherent or chaotic variability), which has been documented in YSOs (e.g., Rucinski et al. 2008) and may be driven, for instance, by fluctuations of the accretion rate in the disk (Lyubarskii 1997). Although each class of variables in our sample exhibits a significant internal spread in calculated β indices, stars dominated by irregular variability (“S,” “B,” and “APD”) have typical $\beta \sim 0.4\text{--}0.5$, above the flicker-noise index and close to the $\beta = 0.5$ index that characterizes Brownian noise (random walk). Higher β indices of $\sim 0.6\text{--}0.7$ characterize the typical \mathcal{SF} of regular variables (“P,” “MP,” “QPS,” “QPD”).¹² These values stand between the β index associated with Brownian noise and that expected for an \mathcal{SF} constructed from a sinusoidal time series ($\beta \sim 1$).

Stars classified as “B,” “QPD,” “APD,” and “S” exhibit, in this order, the largest typical \mathcal{SF} values measured at τ_{knee} across the sample, ranging from 10 times to about 2 times those measured (in decreasing order) for stars classified as “P,” “QPS,” and “MP.” The median τ_{knee} measured across our sample is shortest (~ 0.5 days) for stars classified as “P” or “MP,” between 1 day and 2 days for (in increasing order) “QPS,” “B,” and “QPD” stars, and on the order of 3 days for “S” and “APD” stars. To test how similar or dissimilar different variable classes are with respect to the derived \mathcal{SF} parameters, we applied a two-sample Kolmogorov–Smirnov (K-S) test (Press et al. 1992) and a two-sample Anderson–Darling test (Pettitt 1976) to the distributions in β and τ_{knee} obtained for each K2 class. Results of this analysis are reported in Tables 6 (β index) and 7 (τ_{knee} parameter). While the significance that can be achieved when comparing two given classes is somewhat dependent on how populous those classes are (and this varies considerably from one class to another, as can be deduced from Table 3), some interesting indications can be extracted from these statistical tests. The τ_{knee} parameter appears to be the one that discriminates most among different types of variability. A clear distinction is observed between accretion-disk-related variability patterns (bursters, stochastic, dippers) and patterns dominated by spot modulation: in these cases, the p -values from the K-S test indicate that the null hypothesis can be rejected to a significance ≤ 0.05 and often below 1%.¹³ The same results are obtained when using the Anderson–Darling test. The null hypothesis is instead retained for the comparative distributions in τ_{knee} exhibited by “QPS” and “QPD” variables; this suggests that the physical origins for these two categories are at least partly connected. The comparison between different light-curve classes in terms of the β parameter is more inconclusive, but it suggests a marked difference at least between the most irregular variables and the most regular ones.

7. Discussion

7.1. Mass Dependence of Variability in Young Stars

As illustrated in Sections 4.2.3 and 6, the amount of variability exhibited by YSOs in our sample depends strongly on stellar mass or spectral type. This is observed not only

¹² We exclude EBs from this discussion since the predominant variability signatures on those systems arise not from single-star variability but from transit events.

¹³ The higher p -values obtained when the “B” class is involved, compared to those obtained when comparing other classes of irregular versus regular variables, are likely affected by the very small number of stars in our sample with a bursting behavior.

Table 6

Results of a Two-sample K-S Test Applied to the Cumulative Distributions in β Indices Derived from the \mathcal{SF} Analysis for Stars Belonging to Different Variable Classes

	p -values from Two-sample K-S Test						
	APD	B	MP	P	QPD	QPS	S
APD	
B	0.7	
MP	<i>0.05</i>	0.11	
P	0.008	0.03	0.5	
QPD	0.18	0.3	0.9	0.6	
QPS	0.06	0.14	0.9	0.09	0.8		...
S	0.2	0.3	0.0009	0.00007	0.008	0.0013	

Note. The p -values ≤ 0.05 (corresponding to the threshold where the null hypothesis can be rejected at the 5%-level) are reported in italics. The values highlighted in boldface correspond to cases where the null hypothesis is also rejected at the 5% level according to the Anderson–Darling test statistic. The table is symmetric with respect to its diagonal.

within individual categories of light curves with discernible variability patterns but also among light curves classified as nonvariable or flat-line: indeed, as shown in Figure 12 (top right panel), the baseline of photometric fluctuations measured for B and A stars with light curves classified as “N” is systematically lower than that measured for the light curves of flat-line F to K stars. A flat light curve might in principle be associated with YSOs seen in a geometric configuration close to pole-on (i.e., line of sight to the star nearly aligned with the stellar rotation axis), where the side of the star that faces the observer remains essentially the same at different rotational phases. However, if flat-line light curves were driven purely by the geometric viewing angle, we would expect similar fractions of stars classified as “N” to appear at all spectral types, and this is not supported by the data in Table 4. In fact, the fraction of “N” stars is systematically higher among earlier-type¹⁴ stars (down to F spectral types) than among later-type (G, K) stars, and this is accompanied by an increase in the fraction of objects with detected modulated behaviors (“P,” “QPS”) from early-type to late-type stars. These results can be interpreted in terms of distinct magnetic properties for young stars of different masses. As mentioned in Section 1, homogeneous spectro-polarimetric surveys of intermediate-mass YSOs (Villebrun et al. 2019) have revealed very few detections of magnetic fields for objects with effective surface temperatures hotter than ~ 6000 K (which correspond to SpT \lesssim mid- to late F; Herczeg & Hillenbrand 2014). When magnetic fields are detected, the complexity of the magnetic field structure appears to increase across the H-R diagram, from cooler and purely convective stars that exhibit largely dipolar and axisymmetric fields to hotter stars with large radiative cores that exhibit more chaotic field configurations with weak dipolar components (Gregory et al. 2012; Hill et al. 2019). As dark starspots are formed at the base of strong stellar magnetic loops that suppress local convective flux motions, we would naturally expect to observe more intense modulated variability when large, localized spots,

¹⁴ Data reported in Table 4 might seem to suggest a possible discrepant behavior for B-type stars, with a large fraction of detected periodic behaviors, and a very low statistical fraction of “N” stars. However, this may be driven by the limited number of B-type stars in our sample, and the light-curve classification for objects belonging to this spectral range is somewhat more uncertain than for other spectral types, as evidenced by the large fraction of sources labeled “U” (unclassifiable).

Table 7Results of a Two-sample K-S Test Applied to the Cumulative Distributions in τ_{knee} Parameters Derived from the \mathcal{SF} Analysis for Stars Belonging to Different Variable Classes

	<i>p</i> -values from Two-sample K-S Test						
	APD	B	MP	P	QPD	QPS	S
APD	
B	0.5	
MP	0.00013	0.013	
P	0.0012	0.05	0.6	
QPD	0.2	0.6	0.00011	0.0002	
QPS	0.03	0.8	0.000016	0.0003	0.16		...
S	0.8	0.4	0.00000012	0.000002	0.10	0.018	

Note. The *p*-values ≤ 0.05 (corresponding to the threshold where the null hypothesis can be rejected at the 5% level) are reported in italics. The values highlighted in boldface correspond to cases where the null hypothesis is also rejected at the 5% level according to the Anderson–Darling test statistic. The table is symmetric with respect to its diagonal.

associated with ordered dipolar fields, are present. Conversely, in a chaotic field configuration where magnetic loops and associated starspots are distributed homogeneously across the stellar surface, the starspot-to-photosphere contrast is expected to be similar at all rotational phases, therefore yielding little modulated variability, irrespective of the stellar inclination (e.g., Kesseli et al. 2016). Our results are consistent with the findings by earlier studies of modulated variability in PMS stars, which noted a marked decrease in the occurrence of spot-induced flux variations from fully convective stars to stars with extended radiative cores within individual populations (e.g., Saunders et al. 2009).

Table 4 also reveals a clear distinction between higher-mass and lower-mass stars with respect to disk-driven variability behaviors. The dependence on spectral class is apparent in particular among burster stars (dominated by intense and short-lived accretion), clustered at A and F spectral types, and dipper stars (dominated by occulting dust in the circumstellar environment), clustered at G and K spectral types. A closer inspection of the \mathcal{SF} trends reconstructed for all light curves labeled as “B” (bursting; see Figure 12, bottom left panel) suggests that the SpT dependence observed for this category of variables may be caused, at least partly, by the small number of objects that match this class of photometric behaviors in our sample and by the fraction of those without an SpT estimate from our analysis in Section 3.1. Indeed, as shown in Figure 12, all stars with a burster-like K2 light curve and with no SpT estimate (marked in gray) exhibit a level of \mathcal{SF} variability that is comparable to, or higher than, what is measured for burster stars with available spectral classification. This feature, combined with the mass-dependent trends in the amount of YSO variability discussed earlier, would place the sources in gray at similar or later spectral classes than the sources with available SpT. Dipper stars with available SpT, on the other hand, delimit the range of \mathcal{SF} properties within which all dipper stars with no spectral classification are also located (Figure 12, middle right and bottom right panels). This suggests that the SpT dependence in dipping behaviors reported in Table 4 is real, and the dipping phenomenon is therefore observed only among later-type stars. A trend analogous to the one observed here had already been noted in earlier studies on dipper YSO variables, albeit targeting less massive regions (Ansdell et al. 2016a), and a detailed discussion on its possible origin has been presented by Bodman et al. (2017). Namely, if the dipping behavior is produced by inner disk warps or dust entrained in accretion streams that corotate with the star (as suggested by the similarity in periodicity measured for dipping events and

modulated variability among “QPD” variables; e.g., Stauffer et al. 2015; McGinnis et al. 2015), the phenomenon is only possible if the disk temperature at the corotation radius is below the dust sublimation temperature, $\sim 1300\text{--}1400$ K (Kobayashi et al. 2011; Nagel et al. 2013). Assuming that the disk temperature close to the inner edge is driven primarily by direct irradiation from the star, the temperature of a disk annulus in Keplerian rotation around the star depends on the stellar size and effective temperature T_{eff} and on the radial distance from the star, which, in turn, is related to the local orbital velocity (hence orbital period) of the disk material. Under these assumptions, we can then estimate the minimum period at which it would be possible to observe photometric signatures of occulting dust.

In Figure 14, we illustrate the T_{eff} -dependent minimum periods on which a dipping behavior can be observed, calculated from Equations (1) and (2) of Bodman et al. (2017), using 0.5–2 Myr theoretical isochrones from the Padova and Trieste Stellar Evolutionary Code (PARSEC) models (Marigo et al. 2017) and the Yale-Potsdam Stellar Isochrones (YaPSI; Spada et al. 2017). This diagram reproduces and expands Figure 2 of Bodman et al. (2017) toward higher T_{eff} values, in order to encompass the entire range of stellar properties relevant to our YSO sample. At any given T_{eff} , a dipping behavior can only take place on timescales above the threshold curve traced for a certain age. Periods shorter than (i.e., below) the curve correspond to orbits that are located too close to the star, where the local temperature is too high to allow dust in nonsublimated form. As the diagram illustrates, for lower-mass stars, the minimum periods required for dust at corotation are on the order of a few days, quite consistent with the rotation rates measured for young, disk-bearing stars (e.g., Venuti et al. 2017; Roquette et al. 2017; Rebull et al. 2020), which indicates that dipping behaviors are indeed to be expected over weeks-to-months-long monitoring campaigns. As we move to higher T_{eff} , however, the period corresponding to the minimum distance from the star where dust can exist increases rapidly, reaching orders of several tens of days by the G-type-to-F-type transition. These timescales lie at the upper end of the range of rotational periods measured among young stellar populations, which suggests that the actual occurrence of dust structures at the corotation radius around more massive stars ought to be rare. As $T_{\text{eff}} \sim 10,000$ K are reached, in the A–B spectral class regime, the minimum period for dust at the corotation radius becomes ~ 100 days for ~ 1 Myr old YSOs, well beyond the typical rotation rates

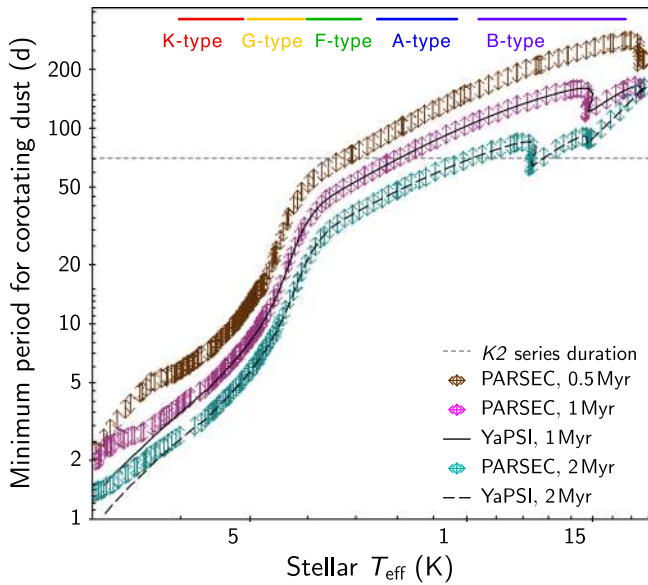


Figure 14. Estimates of the orbital period corresponding to the minimum radial distance from the star at which corotating dust can be present in nonsublimated form, as a function of the temperature of the central star. The double arrows delimit the range of periods calculated, for a given T_{eff} , assuming a dust sublimation temperature of 1300–1400 K, and using stellar parameters (mass, luminosity) tabulated by Marigo et al. (2017; PARSEC isochrones) for 0.5 Myr (brown), 1 Myr (magenta), and 2 Myr (cyan) ages. The average T_{eff} –period estimates derived by using the Spada et al. (2017; YaPSI) model isochrones at 1 Myr (solid line) and 2 Myr (dashed line) are also shown to illustrate the overall agreement between different PMS models as a function of stellar T_{eff} . The total duration of the K2 time series is shown for comparison purposes as a dotted gray line. Horizontal bars on top of the diagram illustrate the approximate T_{eff} ranges for stars in our sample belonging to different spectral classes.

measured for young stars, and beyond the intrinsic timescales that can be probed with our K2 time series.

An additional factor that likely plays a role in the disappearance of dipping behaviors at $\text{SpT} \lesssim G$ is the increasingly complex magnetic field structure for YSOs at the fully convective to partly radiative transition, as discussed earlier. Indeed, as the star–disk interaction is dominated by the dipole component of the magnetic field (which is the component that exhibits the slowest decline in intensity with radial distance from the star; Gregory et al. 2012), a strong dipolar field is crucial to establish a stable accretion regime, which in turn leads to longer-lived accretion structures (inner disk warps, accretion columns) responsible for the repeated occultation events (flux dips) observed on high-inclination star–disk systems (McGinnis et al. 2015, and references therein). As more massive stars ($\gtrsim 2 M_{\odot}$) rapidly develop radiative cores, the magnetic pressure on the inner disk regions decreases and the disk is able to push closer to the star, enhancing the spin-up torque on the central object (Gregory et al. 2012). This scenario hampers further the possibility of ordered dust structures surviving at the corotation radius around early-type stars, as evident from Figure 14.

7.2. Geometries of Star–Disk Interaction in Young Stars

The variety of photometric behaviors identified among disk-bearing YSOs is expected to reflect a range of star–disk interaction phenomena, and coordinated analyses of the color properties characteristic of different behaviors are critical to assess where and how the observed flux variations are triggered

in the star–disk environment. In particular, the IR properties observed for Lagoon Nebula YSOs and depicted in Figure 8 suggest that bursting, stochastic, and dipping behaviors do not share the same origin, although all being driven by disk processes rather than photospheric features.

Burster stars stand out with respect to other disk-bearing variables in their UV (Figure 9, right) and $H\alpha$ (Figure 10, right) excess properties, and they also exhibit the largest IR excesses up to wavelengths $\sim 4.5 \mu\text{m}$ (Figure 8). However, the IR properties at wavelengths longer than $4.5 \mu\text{m}$ appear consistent with the typical color locus for Class II sources, and the characteristic timescales of variability extracted from the K2 light curves for bursters are overall consistent in magnitude with those measured for QPS and QPD variables (Section 6). The IR color trends we observe here for burster stars are supported by those inferred in the study of Findeisen et al. (2013), who used data from Spitzer’s instruments IRAC (3.6–8.0 μm) and MIPS (24 μm) to derive a statistical correlation between IR excess and bursting behaviors at shorter wavelengths but not at longer wavelengths. Taken together, these properties indicate that bursting behaviors are driven by the inner disk. Indeed, magnetohydrodynamic simulations of burst-like variability in YSOs have shown that bursting events are triggered by equatorial accretion tongues that evolve rapidly on the inner disk dynamical timescale (Kulkarni & Romanova 2008, 2009).

Stochastic stars also exhibit a clear association with disk-related activities, notably mass accretion, as indicated by the large fraction of YSOs in this category with enhanced $H\alpha$ emission (Section 4.3.3). However, as shown in Figure 9 (see also Stauffer et al. 2016), they do not exhibit the strong UV excess levels typical of burster stars, which suggests that the erratic behavior of the former may not be driven by the intense accretion regime characteristic of the latter, triggered by instabilities at the inner disk boundary. As mentioned in Section 4.3.1, the colors illustrated in Figure 8 hint at distinctive IR emission properties for stochastic stars, which exhibit the reddest shift compared to other disk-bearing YSOs (including bursters) at the longest wavelengths shown on the diagram (IRAC 5.8–8.0 μm). Similar trends were noted among disk-bearing YSO variables in ρ Ophiucus and Upper Scorpius by Cody & Hillenbrand (2018), who employed IR data from ~ 1.2 to 22 μm and reported a segregation in color between erratic light-curve variables and other (dipper, modulated) light-curve variables at the longest IR wavelengths, but not at near-IR wavelengths, albeit without a clear separation between burster stars and stochastic stars. Similarly, Stauffer et al. (2016) reported a comparable color distribution in IRAC filters for bursters and stochastic stars in the NGC 2264 cluster, with a weak indication of stronger dust contribution for stochastic stars than for burster stars, as indicated by the measured slope of their SEDs between 2 and 8 μm . Strikingly, stochastic stars also appear to exhibit the longest intrinsic timescales of variability from our analysis in Section 6, therefore suggesting that the origin of their photometric behavior may lie in disk regions beyond the inner rim.

To explain the variability observed for stochastic YSOs, Stauffer et al. (2016) hypothesized that the irregular fluctuations trace a time-variable efficiency in funneling mass inward from the disk regions around the outer magnetosphere, beyond the corotation radius, where the gradient in rotational velocity between disk and magnetosphere triggers the ejection of disk

material from the system (propeller regime). A similar mechanism had previously been proposed to explain the accretion variability measured on AA Tau, the prototype for dipper-like YSO variables (Donati et al. 2010), and it had been described theoretically by Romanova et al. (2005). In this scenario, the disk can undergo cyclic variations, being pushed closer to the star and then farther out, following the interaction with the rapidly rotating magnetosphere. A mass exchange occurs between the disk and the stellar magnetospheric region along this cycle, with part of the material being expelled via outflows and a fraction being accreted onto the star. The amount of material successfully channeled toward the star can exhibit rapid variations, with characteristic timescales several times larger than the dynamical timescales of the innermost disk regions (\sim few stellar radii from the star), thus potentially explaining the longer dominant timescales of variability measured for stochastic stars in our sample compared to other types of disk-bearing YSO variables. Interestingly, aperiodic dipper variables in our sample are also found to exhibit dominant timescales of variability of the same order as stochastic stars, and longer than those measured for quasi-periodic dippers, burster stars, and quasi-periodic symmetric variables. This suggests that similar mechanisms of variable accretion, coupled with distinct geometric viewing angles (lower inclinations vs. higher inclinations), may drive stochastic and aperiodic dipping behaviors, while their regular counterparts (QPS and QPD) may be driven by stable accretion, with a steady flow of matter from the inner disk onto the star and a variability pattern modulated by hot spots or accretion structures on the inner disk timescales (e.g., Romanova et al. 2004).

7.3. Stability of the Different Modes of YSO Variability

As reported in Table 3, 80% of Class III objects and nearly 70% of Class II objects in our sample exhibit some degree of periodicity in their light curves. This indicates that the underlying physical causes for their variability are intrinsically stable at least over timescales of months, albeit with smaller-scale irregular variations that can often be observed on top of the repeated variability profiles for disk-bearing stars and that likely trace the structure of individual accretion streams. This is consistent with results from the structure function analysis reported in Section 6, from which dominant timescales of variability on the order of days were extracted across our sample. These findings are mirrored by earlier, long-term monitoring studies of variability in young stars (e.g., Grankin et al. 2007, 2008), which have revealed very stable photometric patterns for disk-free YSOs over multiple years (corresponding to thousands of rotation periods), with subtle variations in the surface spot properties that are reminiscent of the magnetic cycles observed on our Sun (Grankin et al. 2008). Those studies have also revealed a relatively stable typical behavior of young, disk-bearing stars on similar timescales (see also Costigan et al. 2014; Venuti et al. 2015). Venuti et al. (2014) examined the comparative extent of variations in accretion luminosity exhibited by a representative sample of young stars in the NGC 2264 cluster on hour-to-week timescales. They concluded that such variations are dominated by accretion shock modulation along the stellar rotation period, although changes in the accretion rate throughout the disk and close to the star (e.g., Sergison et al. 2020), as well as dust clumps and density perturbations within the disk (e.g., Bouvier et al. 2013),

may induce additional variability beyond the rotational timescales for at least a fraction of Class II YSOs.

To assess the relationship between the characteristic timescales of variability determined for our Lagoon Nebula sample and the actual rotation properties of individual stars, we compared the values of τ_{peak} (which corresponds to the first observed maximum in the \mathcal{SF} , beyond which the \mathcal{SF} typically exhibits a rather flat and oscillatory behavior) with the rotation period of the stars (P_{rot}), measured independently from the K2 light curves as part of a companion paper (Rebull et al., in preparation). This comparison, shown in Figure 15 (top panels), reveals a tight correlation between the two quantities. Similarly, a comparison between the estimated τ_{knee} from \mathcal{SF} power-law fitting (i.e., the intersection between the \mathcal{SF} regimes dominated by direct variability and reflected variability, as detailed in Section 6) and the measured P_{rot} by Rebull et al. (2021 in preparation) exhibits a direct correlation between the two quantities across our sample, as shown in Figure 15 (bottom panels). The typical $P_{\text{rot-to-}\tau_{\text{knee}}}$ ratio is 4.5 ± 1.6 , consistent with what is observed by Sergison et al. (2020) for their sample in the Cep OB3b association.

The photometric measurement of the rotation period of a star from its light curve (via, e.g., the Lomb-Scargle periodogram technique; Scargle 1982) relies on the presence of a repeated luminosity modulation pattern, with a discernible periodicity that can be associated with the rotation motion of the star around its own axis. As discussed in Section 4.1, irregular variables in our sample (“B,” “S,” “APD”) generally do not exhibit any clear periodicity in their light curves, albeit characterized by repeated features. Hence, these categories of stars are not represented in the subsample shown in Figure 15, from which the connection between τ_{knee} and P_{rot} is established. If the same connection can be assumed to be true for all stars, the observed trend in typical τ_{knee} values suggests that stars whose dynamics are dominated by star-disk interaction phenomena (notably “B,” “S,” “QPD,” “APD”) tend to rotate more slowly than stars dominated by geometric modulation by uneven surface features (spots; “P,” “QPS,” “MP”). This is consistent with the distinct distributions of rotation rates that have been reconstructed for several disk-bearing, as opposed to disk-free, young stellar populations (e.g., Venuti et al. 2017; Roquette et al. 2017; Rebull et al. 2018), and it can be understood in the presence of a disk-locking mechanism that prevents the star from spinning up until the inner disk has evolved (e.g., Herbst & Mundt 2005; Vasconcelos & Bouvier 2015; Landin et al. 2016). In any case, our analysis indicates the following:

- (i) for both disk-bearing and disk-free young stars, the most prominent timescale of variability (τ_{knee}) is on the order of days, which corresponds to the rotational timescales;
- (ii) disk-related phenomena exhibit longer variability cycles than the rotation-induced modulated variability observed on YSOs with little, if any, disk-related activity;
- (iii) for every type of variable stars, additional variability beyond $\sim \tau_{\text{knee}}$ timescales and up to timescales of months is typically limited (between 1% and 6-8% of the normalized variability observed up to τ_{knee}).

These conclusions are at least qualitatively consistent with the results obtained by Sergison et al. (2020) in their exploration of a wider range of YSO variability timescales, extending to several years. Of note, those authors reported that

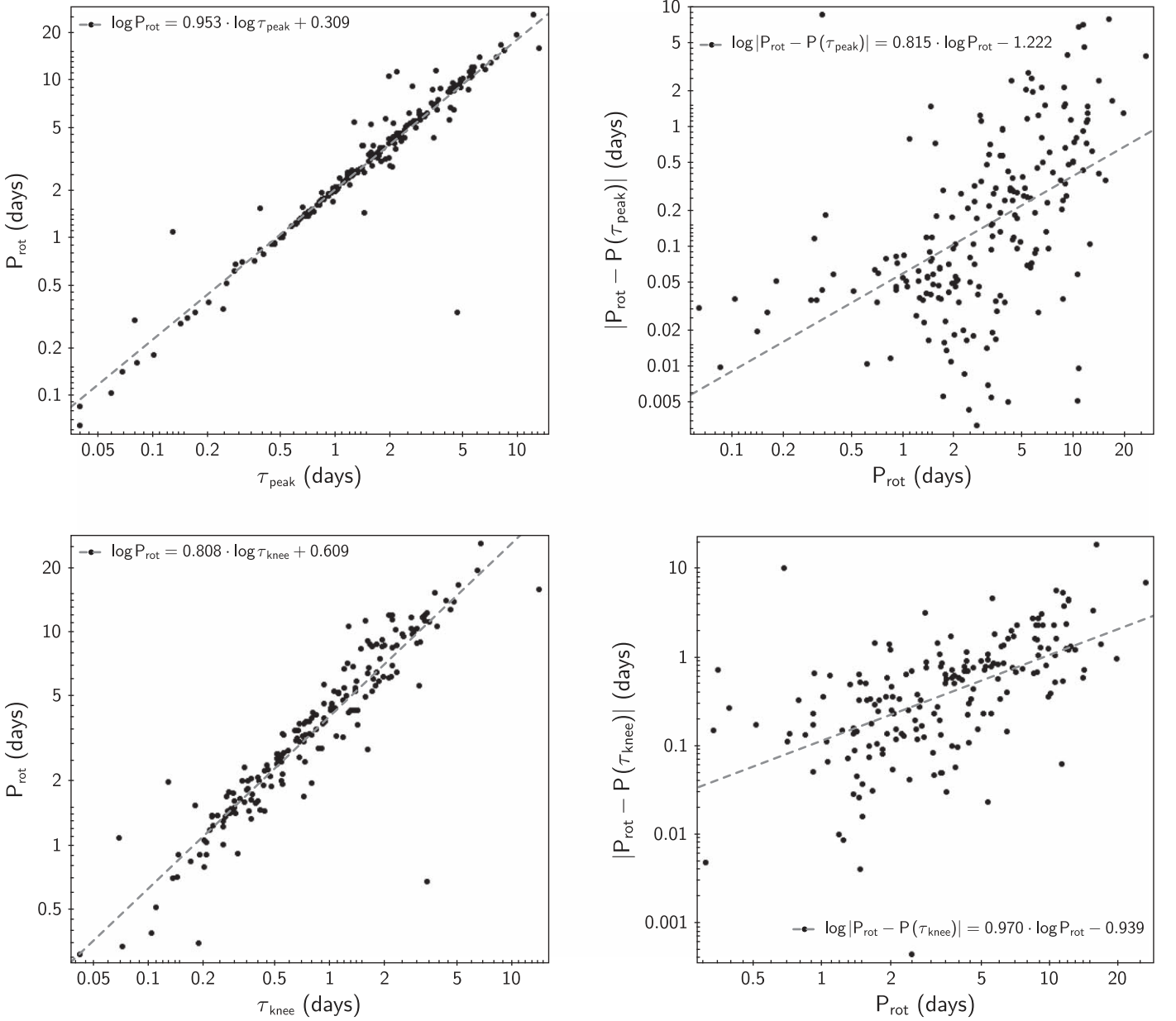


Figure 15. Left: correlation trends between the rotation period P_{rot} measured from the light curves (Rebull et al., 2021 in preparation) and the τ_{peak} (top) and τ_{knee} (bottom) parameters extracted from \mathcal{SF} analysis (see Figure 13). The dashed gray lines trace the logarithmic least-squares fit to the data point distributions, as indicated in the upper left corner of each diagram. Right: absolute residuals between the measured P_{rot} and the period values estimated from τ_{peak} (top) and τ_{knee} (bottom), plotted as a function of P_{rot} . The dashed gray lines mark the logarithmic least-squares fit to the distributions of residuals, as labeled on each diagram.

about one-third of Class II objects in their sample do exhibit additional variability beyond the day-to-week timescales. A discrepancy between the maximum timescale of variability extracted from their structure function analysis and the rotational properties measured for stars in their sample emerges at τ longer than ~ 10 days (see their Figure 14), which corresponds to the upper end of the τ_{knee} range derived here. The Class II objects with long-term variability in the Sergison et al. (2020) sample were found to exhibit smaller amplitudes of variability than Class II objects with no additional variability beyond the rotational timescales. Sergison et al. (2020) concluded that these objects likely exhibit limited modulated variability, due to either complex magnetic field geometries or low-inclination viewing angles to the stars. This reduction in the typically predominant modulated variability would allow

additional sources of variability to emerge on longer time-scales. Interestingly, no $\tau_{\text{knee}} \gtrsim 10$ days were detected in our sample, in spite of our ability to detect intrinsic $\tau \lesssim 35$ days from the K2 light curves (see Section 6). This suggests that any additional variability driven by perturbations or accretion across the disk would manifest on timescales longer than that amount (corresponding to several rotational cycles for these young stars). This, in turn, provides some constraints on the minimum duration of the stability cycles intrinsic to these processes, and/or on the location within the disk where longer-term variability originates. A Keplerian orbit of 35 days corresponds to distances from ~ 0.21 to ~ 0.33 au around stars of masses from 1 to $4 M_{\odot}$, which indicates that longer-term variations on the star may be triggered close to the planet-forming regions of the disks (e.g., Dullemond & Monnier 2010;

Winn & Fabrycky 2015). Albeit at wider orbital distances, hydrodynamical simulations of embedded, Jupiter-mass protoplanets orbiting solar-mass YSOs at distances $\simeq 10$ au (Montesinos et al. 2015) have indeed shown that the radiative feedback from the planet can trigger order-of-magnitude changes in the local disk temperature and accretion rate.

8. Summary and Conclusions

In this study, we have combined high-precision time-series photometry from K2 Campaign 9 with simultaneous multiband monitoring, obtained from the ground with VST/OmegaCAM, to investigate the origin and characteristic timescales of variability exhibited by ~ 1 – 2 Myr old PMS stars in the Lagoon Nebula region. This investigation has allowed us to extend the existing framework for YSO variability studies, established in the course of previous analyses targeting the K to M spectral range, to early-type (B, A) stars, thereby revealing significant trends with stellar mass. We employed the K2 light curves to identify distinct variability classes across our sample, based on the morphology, periodicity, and symmetry of the dominant flux variations observed case by case along the times series. We then mapped the color distribution of the different groups of variables on various photometric diagrams from the UV to the IR, in order to pinpoint the underlying physical drivers.

In agreement with previous studies on star-forming regions such as NGC 2264, ρ Ophiucus, and Upper Scorpius, we identified distinct variability signatures for disk-dominated and photosphere-dominated sources. Irregular light-curve patterns, like bursting, stochastic, or dipping, are observed on stars with large near- and mid-IR excesses, indicative of substantial material in the inner disk environment. Conversely, regular light-curve patterns, like periodic or quasi-periodic, are typically associated with stars that exhibit IR colors similar to the photospheric levels, which indicates more evolved inner disks around these sources. The photometric properties measured in UV and $H\alpha$ filters indicate that the most erratic behaviors (bursting, stochastic) are driven by intense and/or time-variable accretion, while more modest and steady accretion activity is registered on stars with quasi-periodic variability features, either spot modulation or fading events (flux dips) driven by extended accretion curtains or inner disk structures.

While, overall, the vast majority ($\sim 90\%$) of YSOs in our sample exhibit clear variability signatures in their K2 light curves, around one-third of the massive stars (B to F spectral types) do not show any definite variability pattern. A correlated variability analysis between optical and UV wavelengths further indicates that the statistical amount of variability displayed by stars B to early G is indistinguishable from the level of luminosity fluctuations measured for field stars, whereas young stars of later spectral types exhibit significant variability above the field population level. This gradient in the amount of variability measured on early-type versus late-type YSOs is also observed within each individual K2 morphological class, including flat-line light curves, where the intensity of luminosity fluctuations recorded around the typical flux level increases systematically from B and A stars to G and K stars. We suggest that these distinct variability properties for low-mass and high-mass young stars reflect a mass-dependent stellar magnetic field structure: simpler, largely dipolar and axisymmetric magnetic fields for late-type stars, which induce

localized features at the stellar surface, as opposed to more complex and higher-order magnetic fields for early-type stars, which translate to a chaotic (and therefore homogeneous) distribution of surface starspots, with little variability in the spot-to-photosphere ratio at different rotational phases.

Early-type stars in our sample encompass a significantly lower fraction of disk-bearing sources than late-type stars, with a corresponding dearth of disk-dominated variability behaviors. In particular, while erratic light curves like stochastic and bursting are found among more massive (A, F) stars, we do not detect any instance of dipping behaviors at spectral types earlier than G. In the assumption that flux dips are driven by inner disk structures or dust entrained in accretion columns corotating with the star (as indicated by the similarity in intrinsic timescales of variability extracted for dipper light curves and for quasi-periodic light curves dominated by starspot modulation), the lack of dipping behaviors among early-type stars can be understood in terms of their high effective temperatures, which push the dust sublimation radius farther out in the disk, well beyond the star–disk corotating regions. In addition, the absence of a strong dipolar field component in more massive stars would also hamper the development of a stable pattern of star–disk interaction, which is a prerequisite for quasi-periodic accretion features.

Finally, we investigated the dominant timescales of intrinsic variability emerging from the K2 light curves. In agreement with previous studies, we found the day-to-week timescales to be the leading source of intrinsic variability for all YSOs on baselines of at least the months-long timescales probed within a single K2 campaign. However, our results also suggest that distinct variability signatures within this time frame may arise from distinct locations within the star–inner disk environment. Stochastic stars, in particular, exhibit somewhat longer timescales of variability than other disk-dominated sources, and they stand out with their typical mid-IR colors, at the reddest end of the color locus traced by Class II objects. These features suggest that their erratic behavior may be driven by time-variable accretion efficiency on the outer magnetospheric regions, beyond the corotation radius. Aperiodic dipper stars also exhibit timescales of variability comparable to those found for stochastic stars, and their respective color–luminosity trends indicate that these two classes of variables may be triggered by the same physical mechanism (variable mass load onto the accretion column, with consequent rapid evolution of the magnetospheric accretion structures), coupled with different viewing geometries. Burster stars, instead, exhibit typical timescales of variability consistent with those measured for quasi-periodic variables (modulated and dippers), suggesting an origin of the observed variability in the innermost disk regions corotating with the star. The large UV and $H\alpha$ excesses measured here for bursting variables confirm earlier physical explanations of their photometric behavior in terms of intense accretion activity driven by instabilities at the inner disk–magnetosphere boundary.

This study demonstrates the effectiveness of coordinated high-precision and multiwavelength observing campaigns to identify the physical mechanisms that trigger the manifold variability patterns recorded for young stars, in relation to different stellar and circumstellar properties. Many unknowns still remain on how the physics and evolutionary timescales of individual YSOs are influenced by the surrounding environment, in particular by the presence of stellar companions. To

address this issue, we have undertaken a targeted multiplicity survey of young stars in the Lagoon Nebula, guided by the K2 analysis of variability presented here. Results from that survey, which will explore the mass dependence of the early multiplicity fraction and its connection to the star–disk dynamics, will be presented in a subsequent paper.

We wish to thank the anonymous reviewer for a prompt report that helped improve the manuscript’s clarity. We gratefully acknowledge Janet Drew for making her narrowband H α filter available to us for the VST/OmegaCAM observations. L.V.’s research was supported by an appointment to the NASA Postdoctoral Program at the NASA Ames Research Center, administered by Universities Space Research Association under contract with NASA. The work was also supported by the National Aeronautics and Space Administration (NASA) under grant No. 80NSSC21K0633 issued through the NNH20ZDA001N Astrophysics Data Analysis Program (ADAP). This study employed data products from observations made with ESO Telescopes at the La Silla Paranal Observatory under program ID 177.D-3023, as part of the VST Photometric H α Survey of the Southern Galactic Plane and Bulge (VPHAS+; www.vphas.eu). This publication also makes use of data products from the UKIRT Infrared Deep Sky Survey, the Two Micron All Sky Survey, and the Wide-field Infrared Survey Explorer. The Two Micron All Sky Survey is a joint project of the University of Massachusetts and the Infrared Processing and Analysis Center/California Institute of Technology, funded by the National Aeronautics and Space Administration and the National Science Foundation. The Wide-field Infrared Survey Explorer is a joint project of the University of California, Los Angeles, and the Jet Propulsion Laboratory/California Institute of Technology, funded by the National Aeronautics and Space Administration.

Facilities: Kepler/K2, VST (OmegaCAM), Spitzer (IRAC).

Software: TOPCAT (Taylor 2005), NumPy (Oliphant 2006), Scikit-learn (Pedregosa et al. 2011).

ORCID iDs

Laura Venuti  <https://orcid.org/0000-0002-4115-0318>
 Ann Marie Cody  <https://orcid.org/0000-0002-3656-6706>
 Luisa M. Rebull  <https://orcid.org/0000-0001-6381-515X>
 Giacomo Beccari  <https://orcid.org/0000-0002-3865-9906>
 Mike J. Irwin  <https://orcid.org/0000-0002-2191-9038>
 Steve B. Howell  <https://orcid.org/0000-0002-2532-2853>
 Geert Barentsen  <https://orcid.org/0000-0002-3306-3484>

References

Alcalá, J. M., Manara, C. F., Natta, A., et al. 2017, *A&A*, 600, A20
 Alcalá, J. M., Natta, A., Manara, C. F., et al. 2014, *A&A*, 561, A2
 Alencar, S. H. P., Teixeira, P. S., Guimarães, M. M., et al. 2010, *A&A*, 519, A88
 Allen, L. E., Calvet, N., D’Alessio, P., et al. 2004, *ApJS*, 154, 363
 Alonso-Martínez, M., Riviere-Marichalar, P., Meeus, G., et al. 2017, *A&A*, 603, A138
 Andrews, S. M., Wilner, D. J., Zhu, Z., et al. 2016, *ApJL*, 820, L40
 Ansdell, M., Gaidos, E., Rappaport, S. A., et al. 2016a, *ApJ*, 816, 69
 Ansdell, M., Williams, J. P., van der Marel, N., et al. 2016b, *ApJ*, 828, 46
 Antonucci, S., García López, R., Nisini, B., et al. 2011, *A&A*, 534, A32
 Aslan, B., & Zech, G. 2005, *J. Stat. Comput. Simul.*, 75, 109
 Audard, M., Ábrahám, P., Dunham, M. M., et al. 2014, in *Protostars and Planets VI*, ed. H. Beuther et al. (Tucson, AZ: Univ. Arizona Press), 387
 Auvergne, M., Bodin, P., Boisnard, L., et al. 2009, *A&A*, 506, 411
 Baglin, A. 2003, *AdSpR*, 31, 345
 Barenfeld, S. A., Carpenter, J. M., Ricci, L., & Isella, A. 2016, *ApJ*, 827, 142

Barenfeld, S. A., Carpenter, J. M., Sargent, A. I., Isella, A., & Ricci, L. 2017, *ApJ*, 851, 85
 Barentsen, G., Farnhill, H. J., Drew, J. E., et al. 2014, *MNRAS*, 444, 3230
 Barentsen, G., Vink, J. S., Drew, J. E., et al. 2011, *MNRAS*, 415, 103
 Bastian, U., & Mundt, R. 1979a, *A&A*, 78, 181
 Bastian, U., & Mundt, R. 1979b, *A&AS*, 36, 57
 Biazzo, K., Beccari, G., De Marchi, G., & Panagia, N. 2019, *ApJ*, 875, 51
 Bodman, E. H. L., Quillen, A. C., Ansdell, M., et al. 2017, *MNRAS*, 470, 202
 Bonnarel, F., Fernique, P., Bienaymé, O., et al. 2000, *A&AS*, 143, 33
 Borucki, W. J., Koch, D., Basri, G., et al. 2010, *Sci*, 327, 977
 Bouvier, J., Alencar, S. H. P., Bouvier, T., et al. 2007, *A&A*, 463, 1017
 Bouvier, J., Covino, E., Kovo, O., et al. 1995, *A&A*, 299, 89
 Bouvier, J., Grankin, K., Ellerbroek, L. E., Bouy, H., & Barrado, D. 2013, *A&A*, 557, A77
 Broos, P. S., Getman, K. V., Povich, M. S., et al. 2013, *ApJS*, 209, 32
 Calvet, N., & Gullbring, E. 1998, *ApJ*, 509, 802
 Carpenter, J. M., Ricci, L., & Isella, A. 2014, *ApJ*, 787, 42
 Chambers, K. C., Magnier, E. A., Metcalfe, N., et al. 2016, arXiv:1612.05560
 Churchwell, E., Babler, B. L., Meade, M. R., et al. 2009, *PASP*, 121, 213
 Cody, A. M., Barentsen, G., Hedges, C., Gully-Santiago, M., & Cardoso, J. V. D. M. 2018, *RNAAS*, 2, 25
 Cody, A. M., & Hillenbrand, L. A. 2018, *AJ*, 156, 71
 Cody, A. M., Hillenbrand, L. A., David, T. J., et al. 2017, *ApJ*, 836, 41
 Cody, A. M., Stauffer, J., Baglin, A., et al. 2014, *AJ*, 147, 82
 Costigan, G., Vink, J. S., Scholz, A., Ray, T., & Testi, L. 2014, *MNRAS*, 440, 3444
 Covey, K. R., Ivezić, Ž., Schlegel, D., et al. 2007, *AJ*, 134, 2398
 Dahm, S. E. 2008, *Handbook of Star Forming Regions, Volume I: The Northern Sky*, ed. B. Reipurth, Vol. 4 (San Francisco, CA: ASP), 966
 Damiani, F., Prisinzano, L., Micela, G., & Sciortino, S. 2006, *A&A*, 459, 477
 Damiani, F., Prisinzano, L., Micela, G., & Sciortino, S. 2019, *A&A*, 623, A25
 De Marchi, G., Panagia, N., & Romaniello, M. 2010, *ApJ*, 715, 1
 de Vries, W. H., Becker, R. H., & White, R. L. 2003, *AJ*, 126, 1217
 Donati, J. F., Skelly, M. B., Bouvier, J., et al. 2010, *MNRAS*, 409, 1347
 Drew, J. E., Gonzalez-Solares, E., Greimel, R., et al. 2014, *MNRAS*, 440, 2036
 Dullemond, C. P., & Monnier, J. D. 2010, *ARA&A*, 48, 205
 Efron, B., & Tibshirani, R. J. 1993, *An Introduction to the Bootstrap*, Mono. Stat. Appl. Probab (London: Chapman and Hall)
 Fedele, D., Bruderer, S., van Dishoeck, E. F., et al. 2013, *A&A*, 559, A77
 Findeisen, K., Hillenbrand, L., Ofek, E., et al. 2013, *ApJ*, 768, 93
 Flewelling, H. A., Magnier, E. A., Chambers, K. C., et al. 2020, *ApJS*, 251, 7
 Fonseca, N. N. J., Alencar, S. H. P., Bouvier, J., Favata, F., & Flaccomio, E. 2014, *A&A*, 567, A39
 Frasca, A., Manara, C. F., Alcalá, J. M., et al. 2020, *A&A*, 639, L8
 Fruth, T., Kabath, P., Cabrera, J., et al. 2012, *AJ*, 143, 140
 Grankin, K. N., Bouvier, J., Herbst, W., & Melnikov, S. Y. 2008, *A&A*, 479, 827
 Grankin, K. N., Melnikov, S. Y., Bouvier, J., Herbst, W., & Shevchenko, V. S. 2007, *A&A*, 461, 183
 Gregory, S. G., Donati, J. F., Morin, J., et al. 2012, *ApJ*, 755, 97
 Gullbring, E., Hartmann, L., Briceño, C., & Calvet, N. 1998, *ApJ*, 492, 323
 Günther, H. M., Cody, A. M., Covey, K. R., et al. 2014, *AJ*, 148, 122
 Hartmann, L., Herczeg, G., & Calvet, N. 2016, *ARA&A*, 54, 135
 Herbst, W., Herbst, D. K., Grossman, E. J., & Weinstein, D. 1994, *AJ*, 108, 1906
 Herbst, W., & Mundt, R. 2005, *ApJ*, 633, 967
 Herczeg, G. J., & Hillenbrand, L. A. 2014, *ApJ*, 786, 97
 Hill, C. A., Folsom, C. P., Donati, J. F., et al. 2019, *MNRAS*, 484, 5810
 Howell, S. B., Soback, C., Haas, M., et al. 2014, *PASP*, 126, 398
 Howell, S. B., VanOutryve, C., Tonry, J. L., Everett, M. E., & Schneider, R. 2005, *PASP*, 117, 1187
 Hughes, P. A., Aller, H. D., & Aller, M. F. 1992, *ApJ*, 396, 469
 Joy, A. H. 1945, *ApJ*, 102, 168
 Kalari, V. M., Vink, J. S., Drew, J. E., et al. 2015, *MNRAS*, 453, 1026
 Kesseli, A. Y., Petkova, M. A., Wood, K., et al. 2016, *ApJ*, 828, 42
 Kobayashi, H., Kimura, H., Watanabe, S. i., Yamamoto, T., & Müller, S. 2011, *EP&S*, 63, 1067
 Koenig, X. P., & Leisawitz, D. T. 2014, *ApJ*, 791, 131
 Kuhn, M. A., Getman, K. V., Broos, P. S., Townsley, L. K., & Feigelson, E. D. 2013, *ApJS*, 209, 27
 Kuijken, K. 2011, *Msngr*, 146, 8
 Kulkarni, A. K., & Romanova, M. M. 2008, *MNRAS*, 386, 673
 Kulkarni, A. K., & Romanova, M. M. 2009, *MNRAS*, 398, 701
 Kumar, D. L., & Anandarao, B. G. 2010, *MNRAS*, 407, 1170
 Kurosawa, R., Harries, T. J., & Symington, N. H. 2006, *MNRAS*, 370, 580
 Kurosawa, R., & Romanova, M. M. 2013, *MNRAS*, 431, 2673

- Lada, C. J. 1987, IAU Symp. 115, Star Forming Regions, ed. M. Peimbert & J. Jugaku (Dordrecht: Reidel), 1
- Landin, N. R., Mendes, L. T. S., Vaz, L. P. R., & Alencar, S. H. P. 2016, *A&A*, **586**, A96
- Lawrence, A., Warren, S. J., Almaini, O., et al. 2007, *MNRAS*, **379**, 1599
- Lyubarskii, Y. E. 1997, *MNRAS*, **292**, 679
- Manara, C. F., Beccari, G., Da Rio, N., et al. 2013a, *A&A*, **558**, A114
- Manara, C. F., Testi, L., Rigliaco, E., et al. 2013b, *A&A*, **551**, A107
- Marigo, P., Girardi, L., Bressan, A., et al. 2017, *ApJ*, **835**, 77
- McGinnis, P. T., Alencar, S. H. P., Guimarães, M. M., et al. 2015, *A&A*, **577**, A11
- McKee, C. F., & Ostriker, E. C. 2007, *ARA&A*, **45**, 565
- Meyer, M. R., Calvet, N., & Hillenbrand, L. A. 1997, *AJ*, **114**, 288
- Montesinos, M., Cuadra, J., Perez, S., Baruteau, C., & Casassus, S. 2015, *ApJ*, **806**, 253
- Morales-Calderón, M., Stauffer, J. R., Hillenbrand, L. A., et al. 2011, *ApJ*, **733**, 50
- Morau, E., Artemenko, S., Bouvier, J., et al. 2013, *A&A*, **560**, A13
- Morbidelli, A., & Raymond, S. N. 2016, *JGRE*, **121**, 1962
- Nagel, E., D'Alessio, P., Calvet, N., Espaillat, C., & Trinidad, M. A. 2013, *RMxAA*, **49**, 43
- Oliphant, T. E. 2006, A Guide to NumPy, 1 (USA: Trelgol Publishing)
- Oliveira, J. M., & van Loon, J. T. 2004, *A&A*, **418**, 663
- Pasquini, L., Avila, G., Allaert, E., et al. 2000, *Proc. SPIE*, **4008**, 129
- Pedregosa, F., Varoquaux, G., Gramfort, A., et al. 2011, *J. Mach. Learn. Res.*, **12**, 2825, <https://www.jmlr.org/papers/v12/pedregosa11a.html>
- Pettitt, A. N. 1976, *Biometrika*, **63**, 161, <http://www.jstor.org/stable/2335097>
- Povich, M. S., Kuhn, M. A., Getman, K. V., et al. 2013, *ApJS*, **209**, 31
- Preibisch, T., & Mamajek, E. 2008, Handbook of Star Forming Regions, Volume II: The Southern Sky, ed. B. Reipurth, Vol. 5 (San Francisco, CA: ASP), 235
- Press, W. H. 1978, *ComAp*, **7**, 103
- Press, W. H., Teukolsky, S. A., Vetterling, W. T., & Flannery, B. P. 1992, Numerical Recipes in C, The Art of Scientific Computing (Cambridge: Cambridge Univ. Press)
- Prisinzano, L., Damiani, F., Kalari, V., et al. 2019, *A&A*, **623**, A159
- Prisinzano, L., Damiani, F., Micela, G., & Sciortino, S. 2005, *A&A*, **430**, 941
- Rebull, L. M., Stauffer, J. R., Bouvier, J., et al. 2016, *AJ*, **152**, 113
- Rebull, L. M., Stauffer, J. R., Cody, A. M., et al. 2018, *AJ*, **155**, 196
- Rebull, L. M., Stauffer, J. R., Cody, A. M., et al. 2020, *AJ*, **159**, 273
- Rebull, L. M., Stauffer, J. R., Hillenbrand, L. A., et al. 2017, *ApJ*, **839**, 92
- Rigliaco, E., Natta, A., Randich, S., Testi, L., & Biazzo, K. 2011, *A&A*, **525**, A47
- Robberto, M., Soderblom, D. R., Scandariato, G., et al. 2010, *AJ*, **139**, 950
- Robitaille, T. P., Whitney, B. A., Indebetouw, R., & Wood, K. 2007, *ApJS*, **169**, 328
- Romanova, M. M., Lii, P. S., Koldoba, A. V., et al. 2019, *MNRAS*, **485**, 2666
- Romanova, M. M., Ustyugova, G. V., Koldoba, A. V., & Lovelace, R. V. E. 2004, *ApJ*, **610**, 920
- Romanova, M. M., Ustyugova, G. V., Koldoba, A. V., & Lovelace, R. V. E. 2005, *ApJL*, **635**, L165
- Roquette, J., Alencar, S. H. P., Bouvier, J., Guarcello, M. G., & Reipurth, B. 2020, *A&A*, **640**, A128
- Roquette, J., Bouvier, J., Alencar, S. H. P., Vaz, L. P. R., & Guarcello, M. G. 2017, *A&A*, **603**, A106
- Rucinski, S. M., Matthews, J. M., Kuschnig, R., et al. 2008, *MNRAS*, **391**, 1913
- Saunders, E. S., Naylor, T., Mayne, N., & Littlefair, S. P. 2009, *MNRAS*, **397**, 405
- Scargle, J. D. 1982, *ApJ*, **263**, 835
- Schneider, P. C., Günther, H. M., & France, K. 2020, *Galax*, **8**, 27
- Sergison, D. J., Naylor, T., Littlefair, S. P., Bell, C. P. M., & Williams, C. D. H. 2020, *MNRAS*, **491**, 5035
- Shu, F. H., Adams, F. C., & Lizano, S. 1987, *ARA&A*, **25**, 23
- Sicilia-Aguilar, A., Henning, T., & Hartmann, L. W. 2010, *ApJ*, **710**, 597
- Simonetti, J. H., Cordes, J. M., & Heeschen, D. S. 1985, *ApJ*, **296**, 46
- Skrutskie, M. F., Cutri, R. M., Stiening, R., et al. 2006, *AJ*, **131**, 1163
- Sousa, A. P., Alencar, S. H. P., Bouvier, J., et al. 2016, *A&A*, **586**, A47
- Spada, F., Demarque, P., Kim, Y. C., Boyajian, T. S., & Brewer, J. M. 2017, *ApJ*, **838**, 161
- Stauffer, J., Cody, A. M., Baglin, A., et al. 2014, *AJ*, **147**, 83
- Stauffer, J., Cody, A. M., McGinnis, P., et al. 2015, *AJ*, **149**, 130
- Stauffer, J., Cody, A. M., Rebull, L., et al. 2016, *AJ*, **151**, 60
- Stauffer, J., Collier Cameron, A., Jardine, M., et al. 2017, *AJ*, **153**, 152
- Stetson, P. B. 1996, *PASP*, **108**, 851
- Sung, H., Chun, M.-Y., & Bessell, M. S. 2000, *AJ*, **120**, 333
- Taylor, M. B. 2005, in ASP Conf. Ser., 347, Astronomical Data Analysis Software and Systems XIV, ed. P. Shopbell, M. Britton, & R. Ebert, 29
- Teixeira, G. D. C., Kumar, M. S. N., Smith, L., et al. 2018, *A&A*, **619**, A41
- Tohill, N. F. H., Gagné, M., Stecklum, B., & Kenworthy, M. A. 2008, Handbook of Star Forming Regions, Volume II: The Southern Sky, ed. B. Reipurth, Vol. 5 (San Francisco, CA: ASP), 533
- van den Ancker, M. E., The, P. S., Feinstein, A., et al. 1997, *A&AS*, **123**, 63
- Vasconcelos, M. J., & Bouvier, J. 2015, *A&A*, **578**, A89
- Venuti, L., Bouvier, J., Cody, A. M., et al. 2017, *A&A*, **599**, A23
- Venuti, L., Bouvier, J., Flaccomio, E., et al. 2014, *A&A*, **570**, A82
- Venuti, L., Bouvier, J., Irwin, J., et al. 2015, *A&A*, **581**, A66
- Villebrun, F., Alecian, E., Hussain, G., et al. 2019, *A&A*, **622**, A72
- Vrba, F. J., Chugainov, P. F., Weaver, W. B., & Stauffer, J. S. 1993, *AJ*, **106**, 1608
- Walker, G., Matthews, J., Kuschnig, R., et al. 2003, *PASP*, **115**, 1023
- Werner, M. W., Roellig, T. L., Low, F. J., et al. 2004, *ApJS*, **154**, 1
- White, R. J., & Basri, G. 2003, *ApJ*, **582**, 1109
- Wilking, B. A., Gagné, M., & Allen, L. E. 2008, Handbook of Star Forming Regions, Volume II: The Southern Sky, ed. B. Reipurth, Vol. 5 (San Francisco, CA: ASP), 351
- Williams, J. P., & Cieza, L. A. 2011, *ARA&A*, **49**, 67
- Winn, J. N., & Fabrycky, D. C. 2015, *ARA&A*, **53**, 409
- Wright, E. L., Eisenhardt, P. R. M., Mainzer, A. K., et al. 2010, *AJ*, **140**, 1868
- Wright, N. J., Jeffries, R. D., Jackson, R. J., et al. 2019, *MNRAS*, **486**, 2477